CLIMATOLOGY

# Trans-basin linkages prolong Northwestern Pacific marine heatwaves through a circumglobal wave pattern

**Yu Zhao[1] and Jin-Yi Yu[1,2]***



**Marine heatwaves in the Northwestern Pacific (NWP) have become increasingly frequent and persistent, yet the mechanisms enabling their multiseasonal duration remain poorly understood. Through observational analyses and climate model experiments, we demonstrate that NWP marine heatwaves are primarily driven by a quasistationary wavenumber 5 circumglobal wave (CGW) pattern that operates independently of El Niño–Southern Oscillation. The CGW modulates surface heat fluxes during summer, triggering a self-reinforcing feedback loop where NWP warming intensifies the CGW pattern, amplifying and prolonging heatwaves across extended warm seasons. Additionally, CGW-driven summer warming in the northern North Atlantic persists into winter through oceanic thermal inertia, exciting a great-circle wave pattern that propagates back to the NWP, sustaining heatwaves through cold seasons. This interplay between atmospheric waves and trans-basin interactions enables multiyear marine heatwave events. Analysis of observational data and climate model simulations reveals a strengthening CGW influence in recent decades, indicating more frequent and prolonged NWP marine heatwaves under ongoing global warming.**

## INTRODUCTION

In the Northwestern Pacific (NWP), marine heatwaves (MHWs) have exhibited a marked increase in both frequency and intensity over recent decades (*1*–*3*). Many of these events exhibit exceptional persistence, spanning multiple seasons or even extending across several years (*1*–*6*). Such prolonged MHWs exert profound impacts, disrupting marine ecosystems, reducing fisheries productivity, and modulating regional climate, thereby posing substantial threats to biodiversity and coastal economies reliant on marine resources (*7*–*11*). Elucidating the physical mechanisms driving prolonged NWP MHWs is thus critical for improving predictive capability, informing climate adaptation strategies, and enhancing marine resource management (*2*, *12*, *13*).

Existing frameworks for MHW formation focus on local atmospheric forcing (*2*, *13*–*16*), oceanic processes (*17*–*20*), and remote influences from major climate variability modes (*3*, *5*, *21*–*24*). Consistent with these, studies attribute NWP MHWs to persistent high-pressure systems that reduce cloud cover, enhance solar radiation absorption, and suppress latent heat loss. Enhanced atmospheric stability under high-pressure conditions suppresses surface winds, which decreases latent heat flux (*25*–*27*). Other research highlights the role of ocean circulation changes, particularly anomalous transport through western boundary currents (*25*, *28*, *29*). Several studies also identify the El Niño–Southern Oscillation (ENSO) as a key driver, with La Niña conditions fostering anticyclonic atmospheric patterns that promote NWP warming (*24*, *30*).

Yet, as noted earlier, several NWP MHWs (*6*) demonstrate remarkable persistence despite the strong seasonality of the extratropical atmosphere (*31*) and weak ocean-atmosphere coupling in mid-latitudes (*32*), both of which generally act to disrupt sustained ocean warming. Notably, events like the 2018–2023 MHW have persisted across both El Niño and La Niña phases, suggesting that mechanisms beyond local processes and tropical forcing, central to conventional NWP MHW dynamics, also contribute (*6*, *27*, *33*). Recent studies show that anomalous high-pressure systems driving Northeastern Pacific MHWs, particularly around the Gulf of Alaska, are embedded within planetary-scale wave trains, facilitating MHW development through trans-basin interactions (*23*, *34*). These findings suggest that similar atmospheric wave dynamics and trans-basin teleconnections may underpin the prolonged duration of NWP MHWs, offering a perspective to understand their persistence beyond traditional frameworks.

Building on this, we propose that the circumglobal wave (CGW) pattern, also known as the circumglobal teleconnection pattern (*35*, *36*), drives the extended duration of NWP MHWs. This prominent summer circulation feature spans the Northern Hemisphere mid-latitude band (*36*). While prior studies have linked the CGW to terrestrial extreme weather—such as heatwaves in Europe, Asia, and North America (*37*–*41*)—its role in NWP MHW dynamics remains underexplored. Given that CGW activity peaks during boreal summer, aligning with the documented maximum in NWP MHW intensity and frequency (*25*, *42*–*46*), it provides a compelling mechanism for initiating and sustaining these events beyond local forcing alone.

Through observational analyses, model experiments, and Coupled Model Intercomparison Project Phase 6 (CMIP6) historical simulations, we demonstrate that the CGW pattern not only initiates NWP MHWs in summer but also sustains them through trans-basin interactions. The CGW's hemispheric structure simultaneously drives sea surface temperature anomalies (SSTAs) in the North Atlantic during summer alongside MHWs in the NWP. Those Atlantic SSTAs persist into winter, exciting a great-circle wave pattern that propagates back to the NWP, extending MHWs from warm seasons (summer and fall) through cold seasons (winter and spring). Together, these two mechanisms enable NWP MHW persistence across seasons and, when repeated across consecutive years, drive multiyear events. Moreover, we find that the CGW's influence on NWP MHWs has intensified under recent climate change. Crucially, these extratropical wave dynamics operate largely independently of ENSO, underscoring the need to expand conventional MHW frameworks to include hemispheric-scale atmospheric variability in understanding future extremes in the NWP.

[1]Department of Earth System Science, University of California, Irvine, CA, USA. [2]Department of Atmospheric Sciences, National Central University, Taoyuan City, Taiwan.
*Corresponding author. Email: jyyu@uci.edu

## RESULTS

### NWP MHWs: Seasonality and connection to the CGW pattern

The spatial pattern of NWP MHWs is revealed by regressing monthly SSTAs onto the area-averaged SSTAs over the NWP region (the NWP index; see Methods). This regression highlights a distinct warming signal centered in the NWP, with the most intense anomalies situated east of Japan (Fig. 1A). The warming extends southeastward into the central North Pacific, forming an elongated pattern indicative of large-scale atmospheric and oceanic influences. Analysis of the NWP index from 1870 to 2023 shows strong seasonal phase locking, with variance peaking consistently in late boreal summer [July-August-September (JAS)] across all 30-year segments throughout the period (Fig. 1B). This summer peak corresponds with prior findings that NWP MHWs are most frequent and intense during this season (*42*, *43*, *47*). Enhanced ocean susceptibility to atmospheric forcing during summer, when the shallowest mixed layer concentrates heat flux into minimal heat capacity, amplifies the sea surface temperature (SST) response. Coupled with evidence identifying atmospheric forcing as the

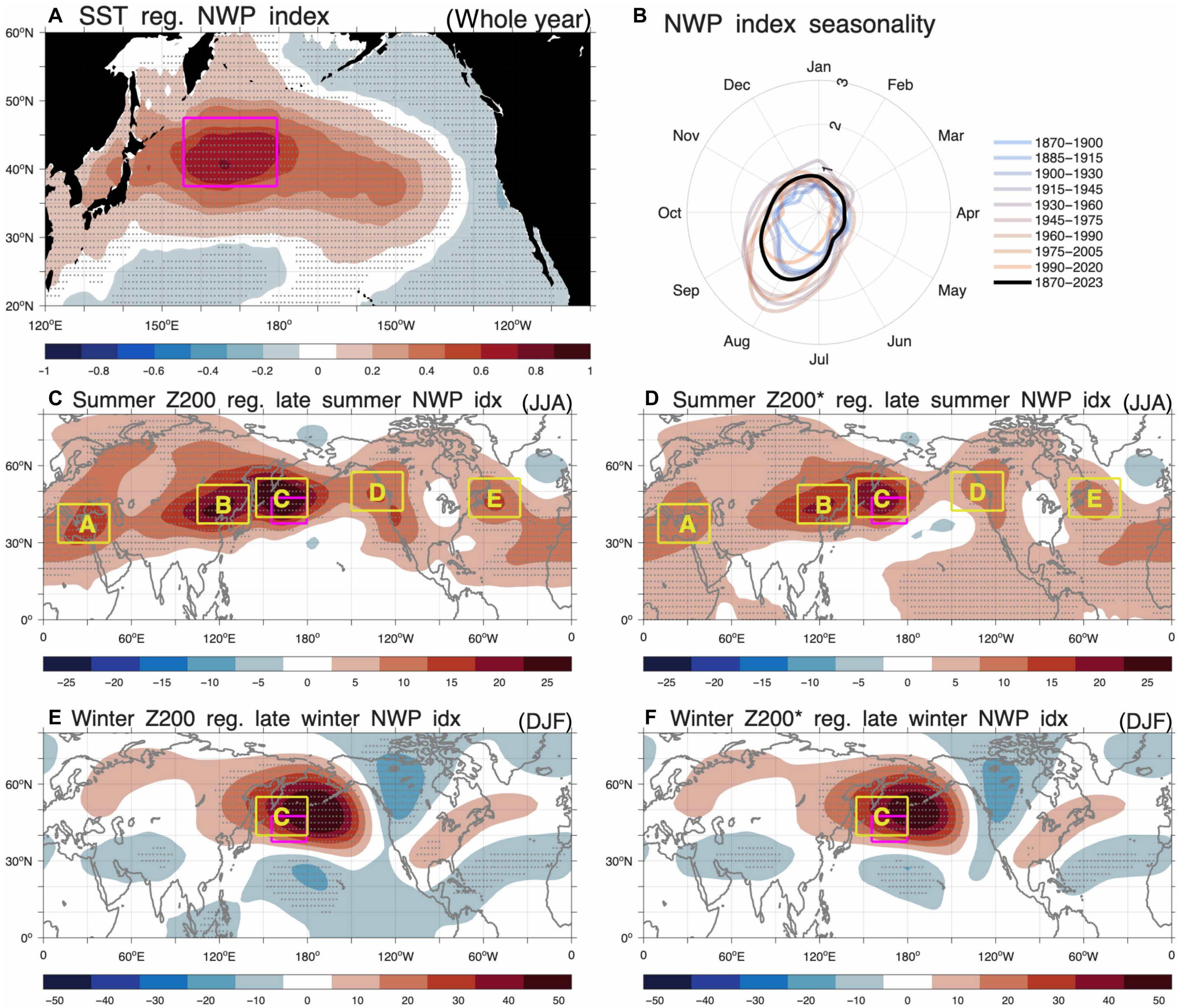


**Fig. 1. NWP MHWs: Pattern, seasonality, and atmospheric circulation patterns across seasons.** (**A**) Sea surface temperature anomaly (SSTA) regression onto the NWP index. (**B**) Seasonality of the NWP index for consecutive 30-year segments (1870–2020, in SDs) and for the full period (1870–2023, black line). (**C**) Summer [June-July-August (JJA)] Z200 regression onto the late-summer [July-August-September (JAS)] NWP index, revealing a CGW pattern with five dominant High centers [(A) to (E), yellow boxes] identified through local maxima. (**D**) Summer Z200* (Z200 anomalies with ENSO signal removed; see Methods) regression onto the same late-summer (JAS) NWP index, showing a similar pattern to (C) with the same five dominant High centers [(A) to (E)]. (**E**) Winter [December-January-February (DJF)] Z200 anomalies regression onto the late winter [January-February-March (JFM)] NWP index, showing a strong high-pressure center over the NWP region (marked as C with yellow box and label). (**F**) Winter Z200* regression onto the late winter NWP index. The NWP region is marked by magenta boxes [(A) and (C) to (F)], and only center C of the CGW pattern is highlighted with yellow label and box in winter panels (E) and (F). Statistical significance at the 95% confidence level is indicated by gray dots. idx, index.

primary driver of NWP MHWs (*6*, *25*–*27*), this pronounced seasonality suggests that summer-specific atmospheric circulation patterns play a dominant role in their formation.

We identified the primary atmospheric driver of summer NWP MHWs by regressing summer [June-July-August (JJA)] 200-hPa geopotential height (Z200) onto the late-summer (JAS) NWP index, applying a 1-month SST lag to account for oceanic response delays. This regression reveals a pronounced wavenumber 5 CGW pattern, marked by an anomalous High center (center C) directly over the NWP MHW region (Fig. 1C). Centers B and C are closely spaced in the jet-exit region. To confirm that they represent dynamically distinct components, rather than a single continuous ridge, we performed local wave activity (LWA) analysis (*48*). The LWA field shows distinct local maxima at both B and C separated by a relative minimum (fig. S1), confirming that they function as separate high-amplitude wave packets. Repeating the analysis on Z200 anomalies with ENSO influences removed (denoted as Z200*; see Methods) reproduces the same CGW signature (Fig. 1D), confirming that these atmospheric dynamics operate largely independently of ENSO. We apply this ENSO-removal framework throughout, except in the final part of Results, where we explicitly compare ENSO's contribution to NWP MHW formation with non-ENSO processes. Spectral analysis of the regressed CGW pattern (fig. S2) further underscores its dominant wavenumber 5 structure, consistent with the five high-pressure centers in Fig. 1D.

We quantify the CGW pattern's strength by defining a CGW index from the five anomalous high-pressure centers identified in the Z200 regression (see Methods). All indices in this study—whether Z200, SST, or CGW—are based on original anomalies. Regressing summer Z200* anomalies onto the CGW index yields a pattern highly correlated [correlation coefficient ($r$) = 0.915, $P < 0.001$, 20°N to 80°N] with that obtained using the NWP index (cf fig. S3 and Fig. 1D). This confirms the CGW index as an effective measure of the strength of the summer atmospheric driver of NWP MHWs. The summer CGW and late-summer NWP indices correlate strongly ($r = 0.740$, $P < 0.001$), underscoring the CGW's primary role in modulating NWP MHWs.

The upper-tropospheric CGW pattern exhibits equivalent barotropic structure, projecting downward to the surface with sea level pressure (SLP) highs, anticyclonic wind anomalies, and positive surface heat flux (SHF) anomalies at center C (figs. S4A and S5). This vertical coupling drives ocean warming through reduced cloud cover, anticyclonic subsidence, and suppressed evaporative cooling—mechanisms consistent with previous NWP MHW studies (*6*). Summer ocean mixed-layer heat budget analysis (see Methods) quantifies this relationship: CGW-driven SHF anomalies account for 77.4% of the total mixed-layer temperature tendency (fig. S5).

To elucidate the mechanisms sustaining the CGW pattern's wavenumber 5 structure and quasistationary nature in summer, we analyzed the waveguide properties of the boreal summer atmosphere (see Methods). Our analysis shows that regions where the stationary wavenumber (*Ks*) exceeds 5 align closely with the summer climatological position of the Northern Hemisphere jet stream, forming a continuous waveguide linking all five anomalous High centers of the CGW (A to E; Fig. 2A). Rossby wave phase speed approaches zero (Fig. 2B), anchoring disturbances where the jet stream decelerates or accelerates. Moreover, localized reductions in the potential vorticity gradient lower *Ks*, creating conditions conducive to quasiresonant amplification of wavenumber 5 disturbances (*39*, *49*, *50*). This quasiresonant state enhances the CGW's coherence and persistence (*51*), thereby maintaining the hemispheric wave pattern through the boreal summer and effectively driving NWP MHWs.

We evaluated the temporal evolution and persistence of the five CGW high-pressure centers by performing lagged regressions of Z200* anomalies onto the summer CGW index. The resulting Hovmöller diagram (30°N to 60°N; Fig. 2C) demonstrates the CGW pattern's quasistationary behavior, with all five centers remaining nearly fixed at their respective longitudes throughout summer, showing minimal propagation. Lagged autocorrelation of the CGW index and Z200* anomalies at centers A to E (Fig. 2D) confirms their temporal stability, with autocorrelation values remaining uniformly high over the season. Together, these waveguide properties and autocorrelation results underscore the CGW's quasistationary nature. Furthermore, these analyses suggest that the summer jet stream's climatological configuration positions the NWP (i.e., center C of the CGW pattern) as a favored region for MHW formation.

### NWP MHW persistence during the extended warm season: Local NWP-CGW self-reinforcing feedback

To assess how long the summer NWP MHWs could last, we calculated the lagged correlation between the monthly NWP index and the summer CGW index, examining the decay characteristics of the NWP MHW's SSTAs after their triggering by the CGW pattern in summer (Fig. 3B). The analysis confirms that NWP-CGW correlation peaks at a 1-month lag, reflecting the ocean's delayed response to atmospheric forcing. Following this peak, the correlation decreases slowly but remains elevated through November. To determine whether this persistence arises solely from oceanic thermal inertia, we applied an AR(1) model (see Methods) to estimate SST persistence driven by ocean memory alone. Comparing the observed lagged NWP-CGW correlation to the AR(1)-predicted persistence reveals that the observed correlation consistently exceeds the AR(1)'s predictions across summer and fall, implying that additional mechanisms, such as local ocean-atmosphere coupling, further sustain NWP warming beyond what thermal inertia can explain.

One potential mechanism sustaining this persistence is a feedback loop wherein NWP MHWs reinforce the anomalous High center that initially triggers them. To explore this bidirectional interaction, we regressed summer Z200* anomalies onto the summer NWP index to evaluate the atmospheric response to NWP SST warming (Fig. 3C). The resulting pattern closely mirrors the CGW that drives the NWP MHWs (cf Fig. 1D), with all five High centers (A to E) spatially aligned. This resemblance suggests that, following initiation of an NWP MHW by the CGW, the resulting SST warming elicits an atmospheric response that strengthens the CGW pattern, amplifying the MHW and establishing a self-reinforcing feedback loop. Through this self-reinforcing feedback loop, the CGW-associated circulation persists into autumn, delaying the decay of warm anomalies and thereby extending MHW duration.

To confirm that NWP MHWs can trigger the CGW pattern, we conducted a forced experiment using NCAR's Atmospheric General Circulation Model (AGCM), in which an idealized Gaussian-shaped SST warming anomaly was imposed over the NWP region (see Methods). The simulated summer Z200 response (Fig. 3D) resembles the observed CGW pattern, displaying five distinct High centers. The equivalent barotropic response extends to the surface, with corresponding SLP highs and anticyclonic wind anomalies at each center (fig. S4B). Center C remains anchored over the NWP, directly reinforcing the regional upper-level ridge. All five CGW high-pressure

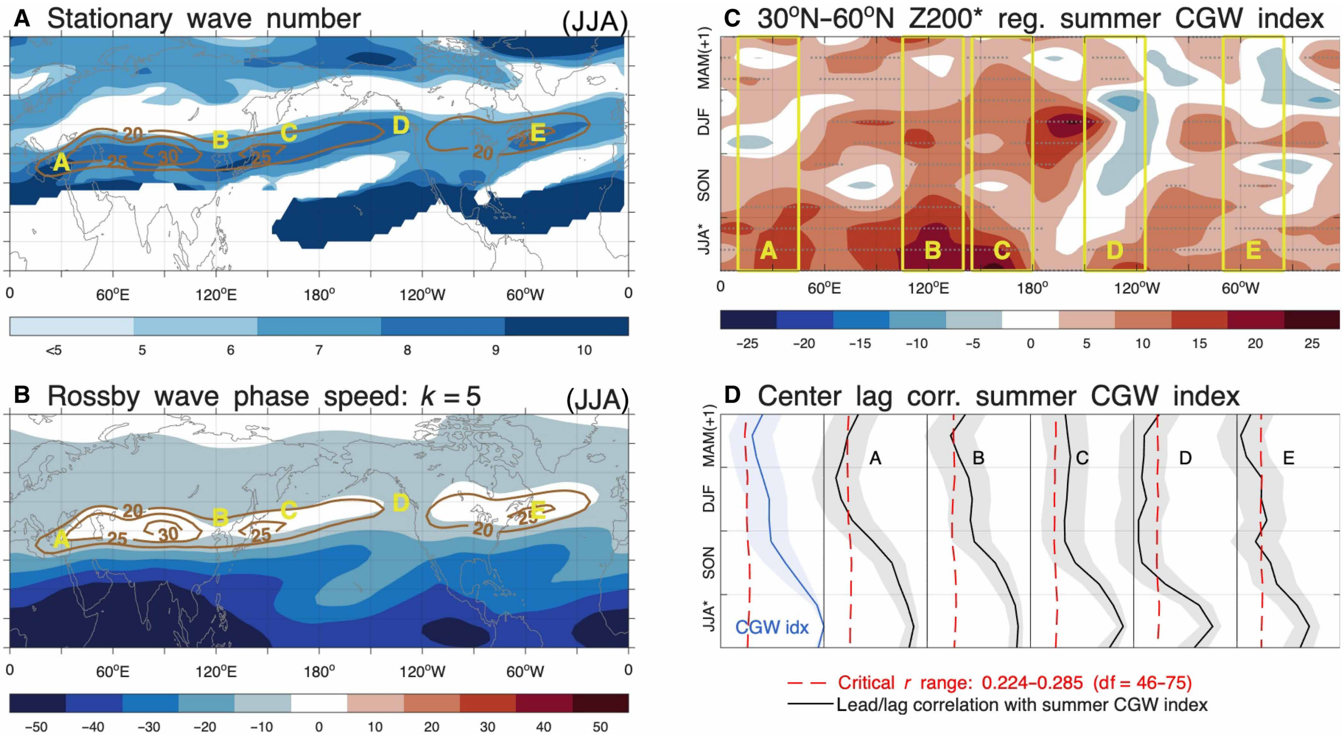


**Fig. 2. Temporal persistence and quasistationary characteristics of the CGW pattern.** (**A**) Summer (JJA) stationary wavenumber. (**B**) Summer Rossby wave phase speed for zonal wavenumber $k = 5$. The CGW centers (A to E), identified from Fig. 1C, are indicated by yellow letters in (A) and (B). Brown contour lines represent climatological 200-hPa zonal wind (U200) [(A) and (B)]. (**C**) Hovmöller diagram of lead-lag Z200* (Z200 anomalies with ENSO signal removed) averaged over 30°N to 60°N regressed onto the summer CGW index, with the five CGW centers indicated. Gray dots denote statistical significance at the 95% confidence level. (**D**) Lead-lag correlation: The blue line shows the CGW index lag correlation with the summer CGW index, whereas black lines represent lag correlations between individual CGW centers (A to E) with the summer CGW index. Shading denotes the 95% confidence interval, and red dashed lines indicate the critical correlation coefficient. SON, September-October-November; MAM, March-April-May.

centers are successfully reproduced in the AGCM experiment, with a hemispheric-scale pattern correlation of 0.45 ($P < 0.01$, 20°N to 80°N). Both results exhibit wavenumber 5 dominance with small phase difference of 39° ($<\pi/4$; fig. S6), confirming that the AGCM successfully reproduces the CGW structure and ocean-atmosphere feedback mechanism over the MHW region. The CGW pattern is likely a quasistationary atmospheric response to MHW-induced warming: Reduced meridional temperature gradients weaken the summer jet stream via thermal wind balance (*52*), amplifying upper-tropospheric wave activity. The summer jet stream's waveguide properties (Fig. 2, A and B) determine both the wavenumber 5 structure and the zonal positions of the five high-pressure centers, with near-zero phase speeds keeping them quasistationary.

The ocean-atmosphere coupling in the NWP region sustains both the NWP MHWs and the CGW pattern. As shown in the Hovmöller diagram (Fig. 2C), Z200* anomalies for all five High centers (except center D) remain significant through summer and fall. Lagged autocorrelation analysis of Z200* anomalies for individual centers (Fig. 2D) further supports this, revealing that anomalies in all centers (except center D) decay slowly, maintaining relatively high correlations from JJA (summer) into at least SON (fall). This prolonged retention of anomalies across most centers aligns with the sustained high values of the CGW index, confirming that the CGW pattern remains a dominant driver of atmospheric circulation throughout the extended warm season (summer and fall).

Collectively, our analyses and experiments reveal clear self-reinforcing feedback: Summer CGW-induced NWP warming strengthens the CGW pattern itself, which further intensifies NWP warming. This positive feedback loop enhances both the persistence and magnitude of NWP MHWs throughout the extended warm season.

### NWP MHW persistence during the extended cold season: Remote trans-basin feedback from the North Atlantic

Lagged correlations between the monthly NWP index and the summer CGW index, presented in Fig. 3B, also reveal that CGW-driven NWP warming persists beyond fall into winter and spring, retaining significant intensity across these seasons. The NWP-CGW correlation remains significant beyond the oceanic thermal inertia's expected decay [*e*-folding time before December in the AR(1) model] and even slightly strengthens during winter and spring. This raises a critical question: How do NWP MHWs survive into winter and spring when the strengthened mid-latitude jets of the cold season should disrupt the summer's quasistationary CGW? As the warm season's NWP-CGW feedback mechanism no longer works, an alternative mechanism must sustain the MHWs during the cold season.

To identify the atmospheric driver of NWP MHWs in winter, we regressed December-January-February (DJF) Z200* anomalies onto the NWP index (Fig. 1F). The resulting pattern no longer resembles the CGW structure observed in summer. Instead, it features a prominent anomalous High over the NWP, closely aligned with center C of

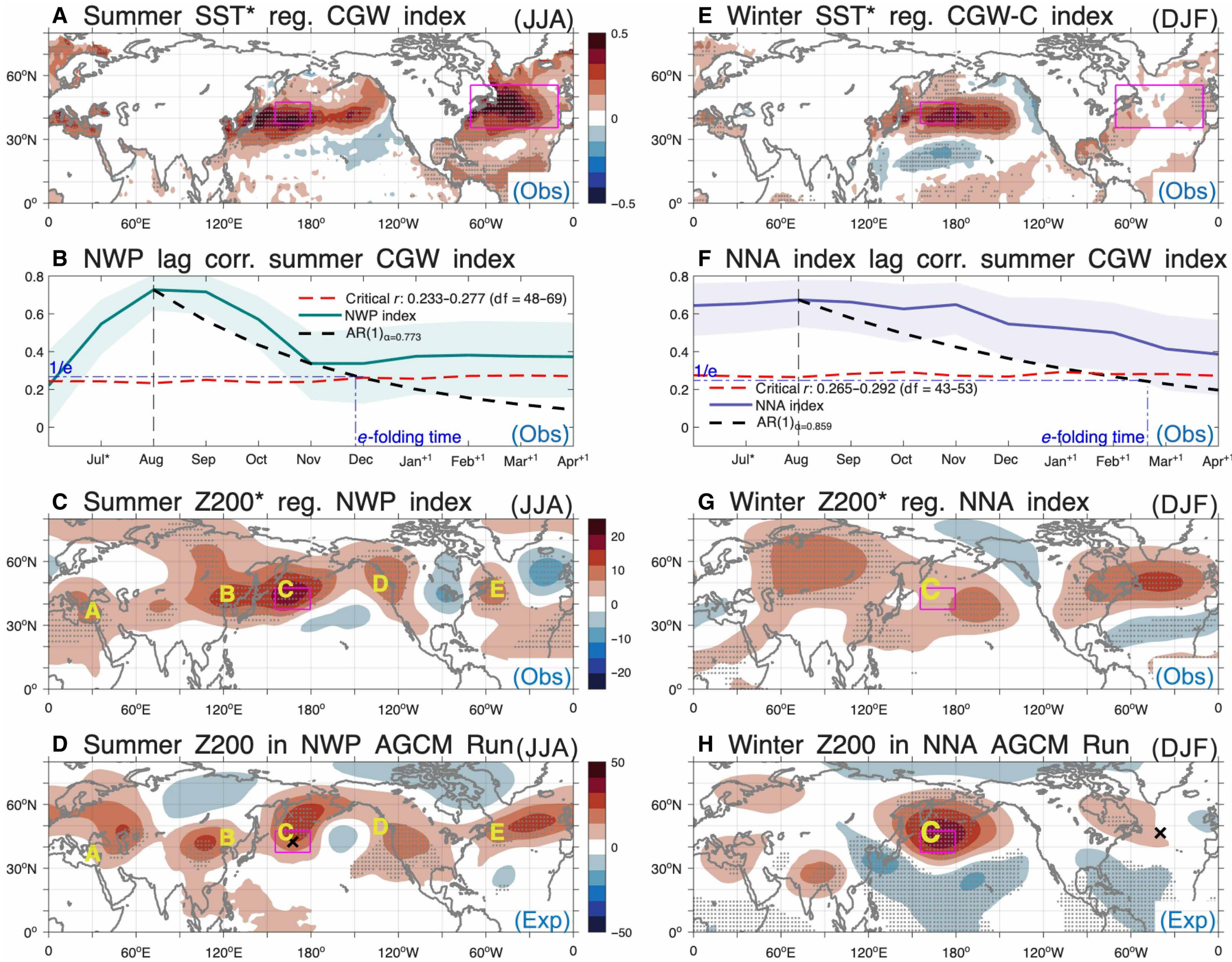


**Fig. 3. Self-reinforcing feedback between NWP warming and the CGW pattern across seasons.** (**A**) Summer (JJA) SST* (SST anomalies with ENSO signal removed) regression onto the summer CGW index. (**B**) Lag correlation between NWP and summer (JJA) CGW indices (green line, shading represents 95% confidence interval), compared to a theoretical decay of an idealized AR(1) model fitted to NWP index (see Methods; dashed black line; $\alpha = 0.773$, with *e*-folding time from peak correlation marked). (**C**) Regression of Summer Z200* (Z200 anomalies with ENSO signal removed) onto the NWP index. (**D**) Summer Z200 response in the NWP Run of forced AGCM experiment. (**E**) Winter (DJF) SST* regression onto the winter CGW-C index. (**F**) Lag correlation between the NNA and summer CGW indices (purple line, shading represents 95% confidence interval), compared to a theoretical decay of an idealized AR(1) model fitted to NNA index (dashed black line; $\alpha = 0.859$, *e*-folding time from peak correlation indicated). (**G**) Winter (DJF) Z200* anomalies regression onto the winter NNA index. (**H**) Winter Z200 response in the NNA Run of forced AGCM experiment. The CGW centers are marked with yellow labels in (C) and (D), and only CGW-C center is marked in (G) to (H). The critical correlation coefficient for significance at the 95% confidence level is marked by the red dashed lines in (B) and (F). Magenta boxes denote the NWP regions in (A), (C) to (E), (G), and (H) and NNA regions in (A) and (E). Statistical significance at the 95% confidence level is indicated by gray dots [(A), (C) to (E), and (G) to (H)]. The forcing center is marked by an "x" in AGCM runs [(D) and (H)]. Obs, observation; Exp, experiment.

the summer CGW pattern (hereafter CGW-C), along with two subsidiary Highs: one extending from the southeastern US into the North Atlantic and another over Eurasia. An identical pattern emerges when regressing raw Z200 anomalies (Fig. 1E), underscoring its robustness. Unlike the quasistationary summer CGW, however, the winter teleconnection experiences greater subseasonal variability from intraseasonal oscillations and regime transitions. This winter pattern raises the question of what maintains it. Barotropic energy conversion analysis (see Methods) reveals negative values at center C when regressed onto the winter NWP index (fig. S7), indicating that synoptic eddies transfer kinetic energy to the time-mean flow, thereby reinforcing and maintaining the winter wave train pattern. This mechanism in the jet-exit region helps sustain the anomalous high-pressure system over NWP MHWs.

We define a CGW-C index to quantify the strength of the anomalous High over the CGW-C region (see Methods). Regression of winter Z200* anomalies onto this index (fig. S8A) reproduces all three anomalous Highs observed in Fig. 1F. A robust correlation between the winter CGW-C and NWP indices ($r = 0.594$, $P < 0.001$) underscores the pivotal role of the CGW-C High in sustaining NWP MHWs during winter. Additionally, the winter mixed-layer heat budget (fig. S9) shows that the CGW-C High drives NWP MHW warming primarily through meridional ocean temperature advection (accounting for 51.2% of the total effect), with SHF playing a smaller role (14.6%), contrasting with summer's SHF-dominated warming pattern.

To investigate the origin of the winter CGW-C High, we regressed winter SST* anomalies onto the CGW-C index (Fig. 3E). This analysis highlighted significant warming in both the NWP and northern North Atlantic (NNA) as linked to the CGW-C High, suggesting that SSTAs in these regions may trigger its formation. In the forced AGCM experiment with an idealized NWP warming (fig. S8B), a high forms over the CGW-C region in winter but remains too confined compared to observations (cf figs. S8A and 1F). In contrast, a forced AGCM experiment with a Gaussian-shaped SSTA warming imposed in the NNA region (see Methods) successfully reproduced both the CGW-C High and a wave train pattern that included additional anomalous Highs over Eurasia and the NNA (Fig. 3H).

Although the AGCM response (Fig. 3H) shows stronger amplitude than the observational NNA-NWP regression (Fig. 3G), this difference likely reflects methodological factors. The 10-member AGCM ensemble filters internal atmospheric variability that may obscure signals in the limited observational record, while the idealized AGCM forcing (1°C coherent Gaussian anomaly) is stronger and more persistent than typical observed NNA conditions. Observational regression limitations from nonlinearity or competing SST forcings could also contribute to the weaker observed relationship. Nevertheless, these results demonstrate that NNA warming is physically capable of generating the observed winter atmospheric pattern, identifying wintertime NNA warming as a critical trigger of the CGW-C High, which, in turn, influences the persistence of NWP MHWs during the cold season.

Because the NNA region lies near Center E of the summer CGW pattern, the winter NNA warming may initially be induced by the summer CGW and then persists into winter. Regressing JJA SST* onto the summer CGW index (Fig. 3A) reveals CGW-associated warming in both the NWP and NNA. Summer ocean mixed-layer heat budget analysis shows that the CGW similarly drives NNA warming through the same SHF process (fig. S10).

The key to understanding the NNA's winter persistence lies in its thermal inertia. The NNA region exhibits substantially deeper mixed layer (~110 versus ~65 m for NWP), which translates to stronger thermal persistence. Lagged autocorrelation analysis (fig. S11) quantifies this: NNA shows significantly stronger lag-1 autocorrelation ($\alpha = 0.857$, $e$-folding time $\tau = 6.5$ months) compared to NWP ($\alpha = 0.773$, $\tau = 3.9$ months), with nonoverlapping 95% confidence intervals confirming statistical significance. This 67% slower decay rate closely matches theoretical predictions based on the MLD ratio: $\ln(\alpha_{\mathrm{NWP}}) / \ln(\alpha_{\mathrm{NNA}}) = 1.69 \approx H_{\mathrm{NNA}} / H_{\mathrm{NWP}} = 1.69$, consistent with the stochastic energy balance model (see Methods). The lagged correlation of the monthly NNA index with the summer CGW index decays slowly from fall through the following spring (Fig. 3F), closely aligning with the expected AR(1) decay rate ($\alpha = 0.859$, $e$-folding time to late February). Lagged SST* regressions confirm persistent NNA warming from summer through winter (fig. S12), sustaining the trans-basin teleconnection that reinforces NWP MHWs during the cold season.

Although the NNA exhibits stronger SST persistence than the NWP due to deeper mixed layers, it does not drive the summer CGW. The summer NNA forcing experiment (fig. S13) produces only localized responses without the hemispheric wavenumber 5 pattern or high over NWP. Thus, the NNA acts as a "seasonal memory keeper": summer CGW warms it, and this persistent warming then drives the winter teleconnection. The NNA AGCM experiment (Fig. 3H) confirms this mechanism: Winter NNA warming generates the CGW-C High and associated wave train. Observational analysis further supports this: Regressing winter Z200* anomalies onto the NNA index (Fig. 3G) reveals a trans-basin wave train with a particularly prominent high-pressure anomaly over center C. The pattern indicates that a great-circle wave train pattern extends from the NNA across northern Eurasia before curving southward into the North Pacific, establishing three distinct High centers: one over the NNA, another over northern Eurasia, and a third over the NWP region. These three centers closely match the dominant Z200* anomaly pattern associated with winter NWP warming (Fig. 1G), confirming that the NNA-driven wave train creates atmospheric conditions conducive to NWP MHWs through the extended cold season (from winter to the following spring).

### Strengthening CGW-MHW linkages under climate change over recent decades

We evaluated whether the CGW forcing, NWP MHWs, and their trans-basin interactions have strengthened over recent decades by examining 1850–2014 simulations from 43 CMIP6 models (table S1) alongside the Twentieth Century Reanalysis (20thC-Reav3). Both the CMIP6 multimodel mean (MMM) and the 20thC-Reanv3 exhibit a wavenumber 5 CGW pattern in summer Z200* regressions onto their NWP indices (fig. S14), closely matching the pattern identified in the National Centers for Environmental Prediction (NCEP)/National Center for Atmospheric Research (NCAR) Reanalysis 1 (used as the observational reference; NCEP-R1) (cf Fig. 1D). This consistency confirms that CMIP6 models effectively capture the observed CGW-driven dynamics of NWP MHWs.

The analysis of the observed and modeled summer CGW index from 1850 to 2014 reveals a pronounced increasing trend across all datasets (Fig. 4A). The CMIP6-MMM, 20thC-Reav3, and NCEP-R1 all demonstrate a significant intensification of CGW activity, particularly from the late 20th century onward. A similar but weaker increasing trend is also observed in the NWP index (Fig. 4B). We further detrended these series and performed a running 30-year correlation between the detrended NWP and CGW indices (Fig. 4C), finding a statistically significant strengthening relationship over time. Since 1970, the correlation has increased at a rate of 0.34 per century in CMIP6-MMM ($P < 0.001$) and 0.12 per century in NCEP-R1 ($P = 0.090$). These increases document a progressively stronger atmosphere-ocean connection in the NWP region. This enhanced coupling suggests that the self-reinforcing feedback mechanism identified in our study has become more efficient, potentially leading to more persistent and intense summer MHWs in this region.

The summer NNA and CGW relationship exhibits an even more pronounced strengthening (Fig. 4D). Since 1970, the 30-year running correlations rise at 0.59 per century ($P < 0.001$) in CMIP6-MMM and 1.04 per century ($P < 0.001$) in 20thC-Reav3, while NCEP-R1 shows a 0.45 per century increase ($P < 0.001$). This marked enhancement of the CGW's influence on NNA SSTAs during summer indicates that the NNA region has become more responsive to CGW forcing in recent decades, facilitating the trans-basin feedback that sustains NWP MHWs during the extended cold season. Winter correlations between the NWP and NNA indices have also strengthened since 1970 across all datasets (Fig. 4E), although values remain below the 95%

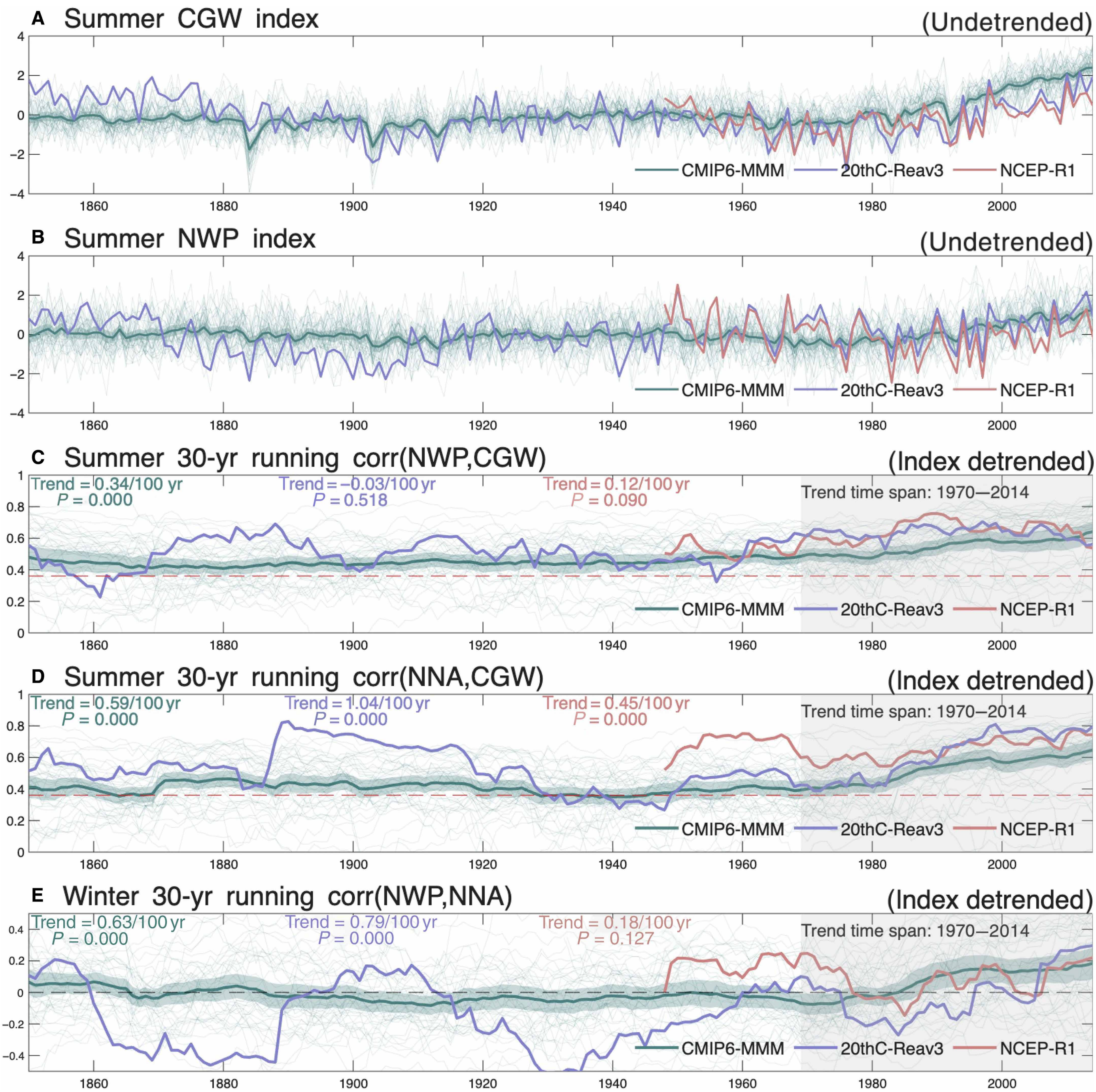


**Fig. 4. Enhanced CGW-NWP relationship under climate change in observations and CMIP6 historical simulations.** (**A**) Time series of normalized undetrended summer (JJA) CGW index from 1850 to 2014 showing CMIP6 multimodel mean (CMIP6-MMM) (thick green line), 20thC-Reav3 (purple), and NCEP/NCAR Reanalysis 1 (NCEP-R1; pink). (**B**) Similar to (A) but for the summer NWP index. (**C**) Thirty-year window running correlation between detrended summer CGW and NWP indices. (**D**) Similar to (C) but showing summer CGW and NNA indices. (**E**) Similar to (C) but showing winter (DJF) NWP and NNA indices. The red dashed lines indicate the critical correlation coefficient (0.367, df = 28) at 95% confidence level. The correlation coefficient trend values from 1970 to 2014 and *P* values are labeled, and the gray areas highlight the trend time span [(C) and (D)]. Light green lines represent individual models, and green shadings represent the 95% confidence interval of CMIP6-MMM. yr, years.

significance threshold (critical $r = 0.367$). This enhanced Atlantic feedback may be associated with the Atlantic multidecadal oscillation (AMO), which shifted from a cold phase peak to a warm phase since the late 1960s, potentially enhancing the NNA's capacity to trigger a trans-basin wave pattern (*53*). This suggests that the trans-basin teleconnection linking NNA conditions to winter NWP warming has likely become more pronounced in recent decades.

To test robustness to different detrending methods, we applied quadratic and EEMD detrending in addition to our primary linear approach (fig. S15 and table S2). The CGW-NNA relationship shows the most robust strengthening across all methods and datasets, with positive trends of 0.30 to 1.04 per century (all $P < 0.001$). The winter NWP-NNA relationship also significantly strengthens in most cases (in seven of the nine method-dataset combinations), with trends of 0.12 to 0.79 per century. The CGW-NWP relationship exhibits greater sensitivity: CMIP6-MMM shows consistent positive trends (0.12 to 0.34 per century), while observations show nonsignificant trends with nonlinear methods. These results demonstrate that trans-basin interactions (CGW-NNA and NWP-NNA) strengthen robustly, while CGW-NWP strengthening is most evident in CMIP6 models and with linear detrending, suggesting influence from broader climate change signals including the overall warming trend and multidecadal variability.

### Evaluating ENSO's role in CGW and NWP MHW mechanisms

Building on studies suggesting that ENSO may modulate or influence the CGW pattern (*54*), primarily through its impact on the Indian summer monsoon (*36*, *55*, *56*), we assessed the tropical Pacific's potential role in shaping NWP MHWs by regressing summer SSTAs onto the NWP index (Fig. 5A). This analysis shows the hallmark NWP warming, accompanied by La Niña–like cooling in the tropical Pacific. Conversely, summer SSTAs regressed onto the cold tongue index (CTI; see Methods) also exhibit NWP warming but with a distinct southeastward extension into the subtropical central Pacific, rather than the full zonal footprint of NWP MHWs (Fig. 5B). This discrepancy suggests that the NWP SST warming pattern associated with or triggered by La Niña does not fully reproduce the observed NWP MHW pattern. Furthermore, regressing Z200 anomalies onto the CTI shows partial alignment with CGW centers (fig. S16), yet the resulting pattern is not dominated by a wavenumber 5 structure (fig. S17), suggesting that ENSO is not the dominant driver of either the CGW pattern or NWP MHWs. Thus, the precise contribution of ENSO forcing to the summer CGW and NWP MHWs merits further investigation.

In the observational record (1948–2024), late-summer NWP and summer CGW indices exhibit a strong positive correlation ($r = 0.740$, $P < 0.001$; Fig. 5C, bottom left), highlighting the CGW's central role in driving NWP MHWs. This relationship persists through both El Niño (CTI > +0.5 SD; warm-colored) and La Niña (CTI < −0.5 SD; cool-colored) conditions, indicating that CGW forcing operates independently of ENSO phase. To disentangle ENSO and CGW contributions, we compared the PDFs of the late-summer NWP index under La Niña (CTI < 0) and positive CGW (CGW > 0) conditions using 1000-sample bootstrap tests with a skewed Gaussian distribution assumption (Fig. 5C, top). A Kolmogorov-Smirnov (KS) test indicates a statistically significant difference between the two PDFs ($P < 0.001$), reinforcing that CGW and ENSO represent separate forcing mechanisms for NWP MHWs. Furthermore, the modal NWP index under positive CGW ($M = 0.364$ SD) is nearly nine times greater than under La Niña ($M = 0.040$ SD), demonstrating that CGW forcing elicits stronger NWP warming than La Niña alone. A similar PDF analysis comparing summer CGW index values under negative CTI and positive NWP conditions (Fig. 5C, bottom right) further demonstrates that local NWP SST warming more effectively amplifies the summer CGW pattern than ENSO forcing. A KS test confirms a significant difference between these distributions ($P < 0.001$), with the CGW index's PDF under positive NWP conditions showing a modal value ($M = 0.444$ SD) that is ~11 times greater than under negative CTI conditions ($M = 0.040$ SD), highlighting that local NWP warming is more efficient at exciting the CGW pattern than La Niña forcing.

We evaluated the influence of ENSO on the summer CGW-NWP relationship by computing both standard and partial correlations among the CTI, NWP, and CGW indices (Fig. 5D). The standard CGW-NWP correlation is 0.740, explaining ~55% of NWP variance; after removing ENSO effects, the partial CGW-NWP correlation remains high ($r = 0.708$), demonstrating that this linkage is largely independent of ENSO. In contrast, the CTI-NWP standard correlation is −0.344 (~10% of variance), and it falls to −0.168 (~3% of variance, $P = 0.181$) once CGW influences are accounted for, rendering it nonsignificant. Similarly, the CTI-CGW correlation drops from −0.321 to −0.104 ($P = 0.406$) when the NWP index is held constant. These results indicate that ENSO contributes only marginally, if at all, to NWP MHWs and CGW variability, whereas the CGW itself stands out as the primary driver of NWP MHWs, largely independent of ENSO forcing.

## DISCUSSION

This study establishes a framework for understanding the formation and persistence of NWP MHWs, emphasizing the pivotal role of extratropical atmospheric wave dynamics and trans-basin interactions. During summer, a quasistationary wavenumber 5 CGW pattern drives NWP warming, which is amplified by a self-reinforcing feedback loop: The CGW triggers NWP warming, which subsequently strengthens the CGW (Fig. 6A). This local ocean-atmosphere coupling sustains MHWs throughout the extended warm half-year. Additionally, trans-basin feedback connects the North Atlantic to the NWP: summer CGW-induced warming in the NNA persists into winter due to oceanic thermal inertia. Following the dissipation of the summer CGW, this lingering winter NNA warming generates a large-scale wave train across Eurasia (Fig. 6B), sustaining NWP MHWs through the extended cold half-year. Collectively, these two seasonal mechanisms explain how NWP MHWs persist across a full annual cycle and, when repeated across consecutive years, drive multiyear events.

Century-long reanalysis datasets (20thC-Reav3), CMIP6 historical simulations, and recent observational data (NCEP-R1) collectively reveal a strengthening of the CGW-NWP interaction and trans-basin feedback since 1970, likely driven by global warming, the AMO's phase shift, or both. These enhancements suggest a potential for increasingly severe, prolonged, and frequent NWP MHWs under continued global warming.

While our AGCM experiments demonstrate that NWP SST anomalies can excite the CGW, we acknowledge that other large-scale factors may also contribute to driving the CGW pattern. Changes in atmospheric circulation due to Arctic amplification (*57*, *58*), aerosol forcing (*59*, *60*), jet stream shifts (*61*), and other processes could influence CGW activity and its relationship with NWP MHWs. A

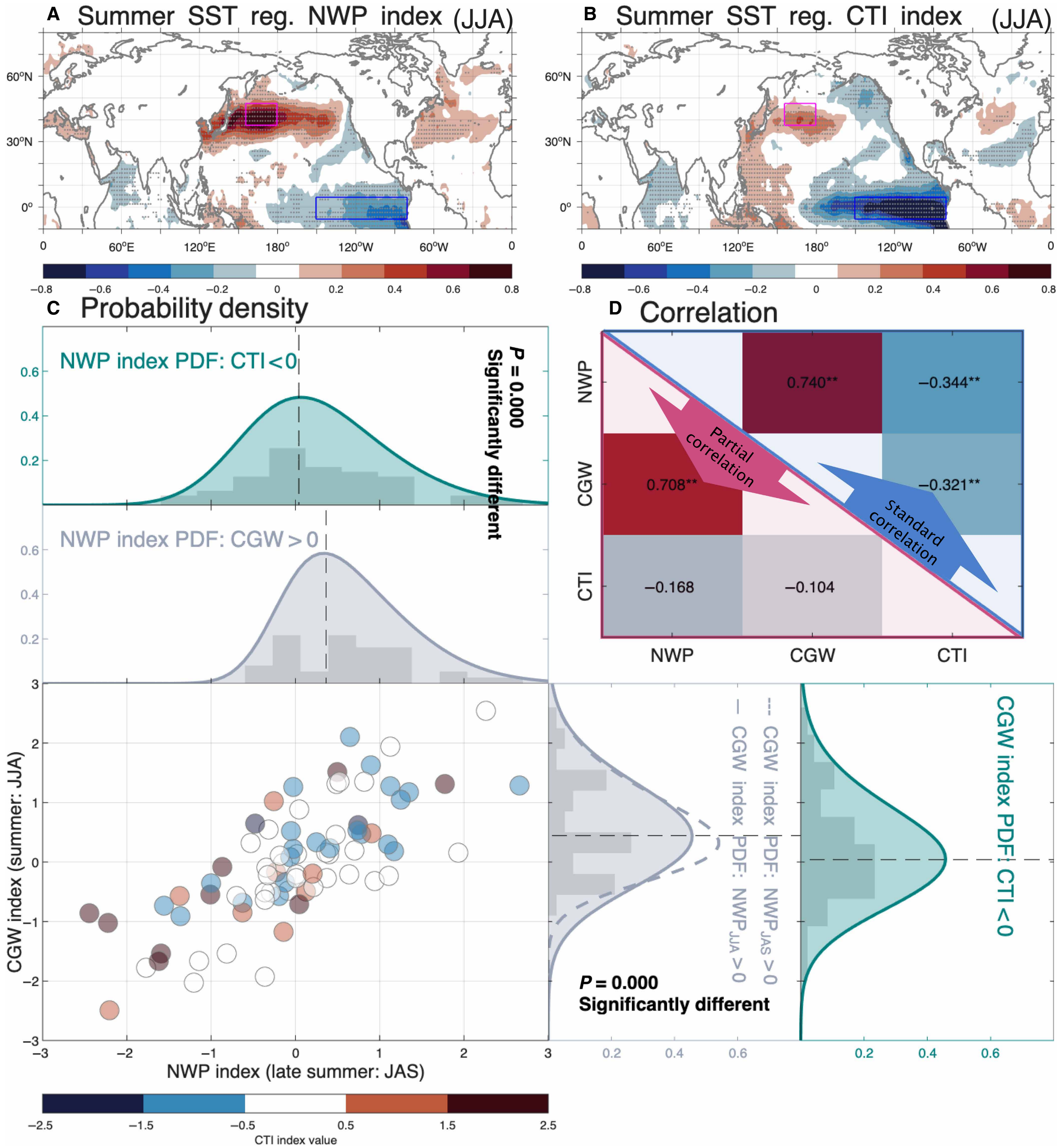


**Fig. 5. CGW dominance over ENSO forcing in driving NWP MHWs in observations.** Summer (JJA) SSTA regression onto (**A**) summer NWP and (**B**) summer CTI indices (multiplied by −1 for comparison). (**C**) The figure contains three elements: (i) Top: Two probability density functions (PDFs) showing late-summer (JAS) NWP under cooling tropical conditions (summer CTI < 0) and positive summer CGW conditions; black dashed lines denote corresponding modal values; (ii) Bottom right: Two PDFs showing summer CGW under cooling summer CTI and warm summer NWP conditions (thick purple dash line indicates warm late-summer NWP conditions); (iii) Bottom left: Scatter plot of yearly values of late-summer NWP versus summer CGW indices, with points colored according to their corresponding summer CTI values. Distributions in (i) and (ii) differ significantly [Kolmogorov-Smirnov (KS) test: $P < 0.001$ for both NWP and CGW]. (**D**) Correlation heatmap between the three indices (standard correlation coefficients in top right, partial correlation coefficients in bottom left), with asterisks marking 99% significance. Magenta boxes indicate the NWP regions, and blue boxes indicate the CTI regions [(A) and (B)]. Gray dots in (A) and (B) denote statistical significance at the 95% confidence level.

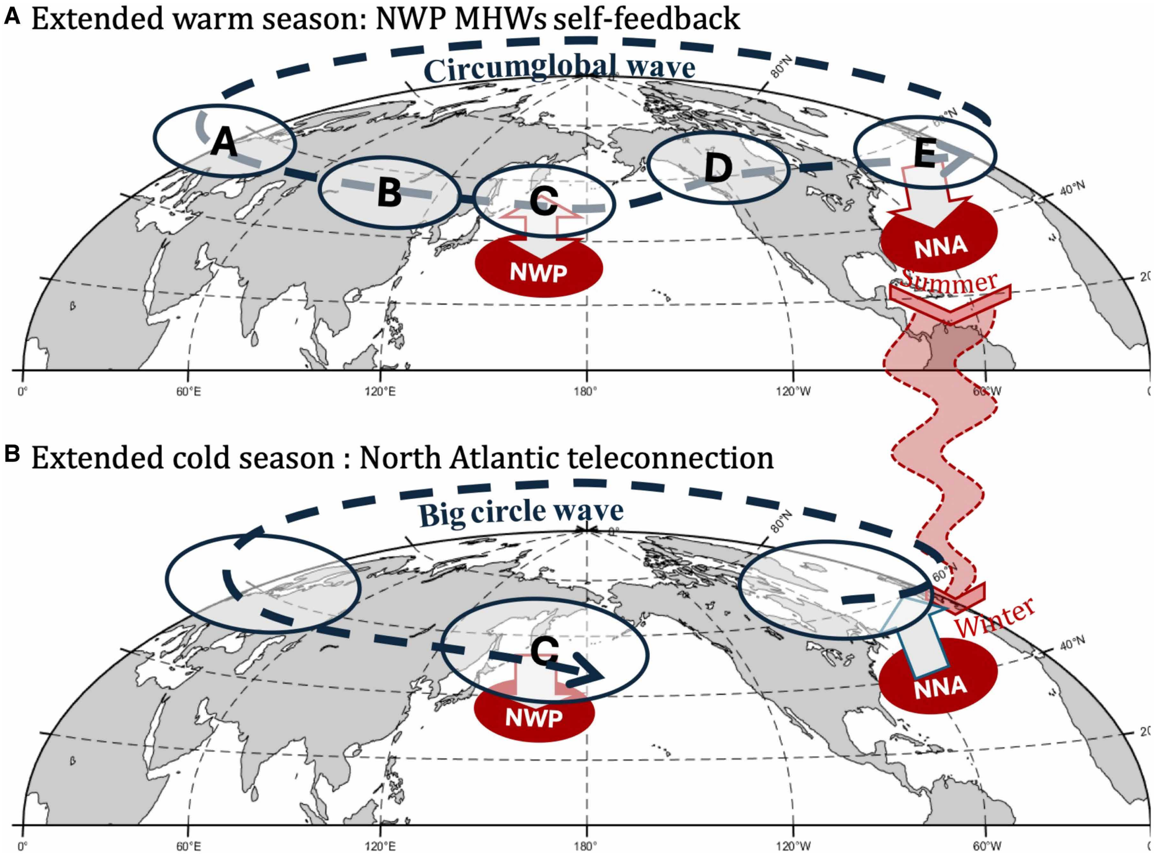


**Fig. 6. Overview of trans-basin feedback mechanisms sustaining NWP MHWs across seasons through extratropical atmospheric waves.** (**A**) Extended warm season self-reinforcing mechanism: The CGW pattern with high-pressure centers A to E drives NWP MHWs. Red arrows between NWP and center C illustrate the self-reinforcing feedback where NWP warming strengthens the CGW pattern. Simultaneously, the CGW drives warming in the NNA, shown by arrows from center E to NNA. (**B**) Extended cold teleconnection: The North Atlantic influences NWP through a great-circle wave pattern. The red arrow shows how high pressure over center C maintains NWP warming, whereas the blue arrow indicates NNA's role in exciting this teleconnection. Both NWP and NNA regions appear highlighted in red. The red-shaded arrow connecting (A) and (B) represents NNA warming persisting through ocean memory into winter. Dashed blue lines trace wave pathways.

comprehensive investigation of the roles of these factors in the CGW-NWP MHW relationship would require extensive additional analyses beyond the scope of the present study. The physical framework that we establish here, demonstrating that ocean-atmosphere coupling in the NWP can excite and sustain the CGW pattern through self-reinforcing feedback, provides a foundation for future investigations into how these additional factors may modulate or enhance this self-reinforcing feedback mechanism.

While our framework explains the mechanisms enabling multi-seasonal and potential multiyear persistence of NWP MHWs, MHW termination occurs when the feedback loops are interrupted by stronger internal atmospheric or oceanic dynamics. During certain years or seasons, internal atmospheric variability may overwhelm the air-sea coupling mechanisms. For example, when the atmosphere's internal dynamics favor anomalous low-pressure conditions over the NWP region rather than the high-pressure anomaly that would normally be induced by warm SSTAs, the summer self-reinforcing feedback cannot be established. Similarly, during winter, if atmospheric internal variability produces circulation patterns that prevent the formation of the expected high-pressure response to NNA warming, then the trans-basin teleconnection fails to sustain the NWP MHW. In such cases, despite the presence of warm SST anomalies in both the NWP and NNA regions, the positive feedback mechanisms are interrupted and the MHW event terminates.

Although our study emphasizes delineating the CGW-NWP and trans-basin feedbacks rather than their root causes, several factors may contribute to these evolving dynamics: decreasing mixed-layer depths that enhance SST-atmosphere coupling (*19*, *20*, *62*, *63*), latitudinal shifts in jet stream location that reshape Rossby wave waveguides (*57*, *61*, *64*), Arctic amplification that weakens meridional temperature gradients and modifies atmospheric wave dynamics (*51*, *57*, *58*, *65*), and changes in North Pacific blocking activities near the NWP region (*50*), among others. Further research is needed to explore the evolving nature of extratropical atmospheric wave dynamics, associated atmosphere-ocean and trans-basin interactions, and their roles in driving ocean extreme events that affect marine ecosystems, fisheries, and coastal communities.

## METHODS

### Observational data

This study uses multiple observational datasets spanning different temporal ranges. We obtained monthly SST data at 1° by 1° spatial resolution from the Hadley Centre Sea Ice and SST dataset (*66*)

(1870 to September 2024). We sourced atmospheric variables, including geopotential height at 200 hPa (Z200), zonal and meridional winds at 200 hPa (U200 and V200), and downward surface shortwave radiation, from NCEP/NCAR Reanalysis (*67*) at 2.5° by 2.5° spatial resolution (1948 to September 2024). We obtained ocean variables essential for mixed-layer heat budget analysis, including mixed-layer depth, potential temperature, horizontal currents, and net SHF, from the Global Ocean Data Assimilation System dataset (*68*) at 1° by 1/3° spatial resolution (1980 to September 2024).

### Historical CMIP6 multimodel data

We analyzed historical simulations from 43 CMIP6 models (*69*) (listed in table S1) covering the period 1850–2014. For consistency, we remapped all model outputs onto a 1° by 1° resolution grid via bilinear interpolation. We extracted surface air temperature (SAT; used as an SST proxy where SST was unavailable) and Z200 for consistency with observational fields.

### The 20th Century Reanalysis V3 data

To extend our long-term perspective, we include the NOAA-CIRES-DOE 20th Century Reanalysis V3 dataset (*70*), spanning from 1850 to 2014, at 1° by 1° spatial resolution. As with CMIP6, we use SAT as a surrogate for SST and analyze Z200.

### Data processing

For all datasets described above, we computed anomalies as deviations from the 1981–2010 seasonal climatology. Linear trends were removed from all variables by default.

### Climate indices

Several key climate indices were constructed to analyze the relationships between MHWs and atmospheric patterns. The NWP index was defined as the area-average SSTAs over the region 37.5°N to 47.5°N, 155°E to 180°E to capture the warming behavior and variability associated with NWP MHWs, rather than applying a formal percentile-based MHW definition. The CGW index was derived by averaging the Z200 anomalies at five key centers (A to E): center A (30°N to 45°N, 10°E to 45°E), center B (37.5°N to 52.5°N, 105°E to 140°E), center C (40°N to 55°N, 145°E to 180°E), center D (42.5°N to 57.5°N, 150°W to 115°W), and center E (40°N to 55°N, 70°W to 35°W). The final CGW index represents the sum of these five normalized center values. Individual center indices (e.g., CGW-C) represent the normalized Z200 anomaly averaged over their respective regions. The CTI was defined as the area-averaged SSTAs over the eastern equatorial Pacific region (6°S to 4°N, 150°W to 80°W). The NNA index was defined as the area-averaged SSTA over the region 35°N to 55°N, 70°W to 10°W. All indices are normalized prior to analysis.

### Statistical significance test

Statistical significance for correlation and regression coefficients was assessed using Student's $t$ test, with degrees of freedom adjusted to account for temporal autocorrelation following (*71*).

To account for the reduction in independent samples due to temporal persistence, we calculated the effective degrees of freedom as

$$N_{\mathrm{eff}} = N \times \frac{1 - r_1 r_2}{1 + r_1 r_2} \quad (1)$$

where $N$ is the sample size, $r_1$ is the lag-1 autocorrelation of the predictor time series, and $r_2$ is the lag-1 autocorrelation of the predictand time series. For spatial regression analyses, $r_2$ represents the lag-1 autocorrelation of the area-averaged predictand field as a conservative estimate. For comparing distributions, the KS test was applied to assess whether two sample distributions significantly differ. All tests were applied at significance levels of $\alpha = 0.05$ or 0.01.

### LWA analysis

To quantify wave amplitude and identify distinct wave packets, we calculated LWA following (*48*). LWA measures the meridional displacement of the jet stream from its zonal-mean position, providing an objective metric for identifying high-pressure/blocking regions.

The LWA is defined as

$$A(\lambda, \phi, t) = \frac{1}{a\cos\phi} \int_{\phi_s}^{\phi} \left(\overline{Q} - Q\right) a\cos\phi' \, d\phi' \quad (2)$$

where $A$ is the LWA, $\lambda$ is longitude, $\varphi$ is latitude, $a$ is Earth's radius, $Q$ is quasigeostrophic potential vorticity (QGPV) at a given pressure level (200 hPa here), $\overline{Q}$ is the zonal mean of QGPV, and $\varphi_s$ is the southern reference latitude.

The QGPV is calculated as

$$Q = f + \frac{1}{a\cos\phi} \frac{\partial v}{\partial \lambda} - \frac{1}{a\cos\phi} \frac{\partial (u\cos\phi)}{\partial \phi} \quad (3)$$

where $f$ is the Coriolis parameter, and $u$ and $v$ are zonal and meridional winds, respectively.

### Wavenumber spectral analysis

To identify the dominant zonal wavenumbers in the atmospheric circulation patterns, we performed spectral analysis on the 200-hPa meridional wind with ENSO signal removed (V200*) regressed onto the corresponding indices. V200* was chosen over Z200* for its better representation of wave-like structures. A fast Fourier transform was applied to these zonal regressions to decompose the spatial anomalies into wavenumber components.

### Ocean mixed-layer heat budget

The mixed-layer temperature tendency equation (*72*) can be expressed as

$$\frac{\partial T_m}{\partial t} = \frac{Q_{net} - Q_{sw}(h)}{\rho c_p h} - \left( \frac{u_m \partial T_m}{\partial x} + \frac{v_m \partial T_m}{\partial y} \right) - w_e \left( \frac{T_m - T_h}{h} \right) + \mathrm{DIFF} \quad (4)$$

where $T_m$ is the potential temperature vertically averaged over the mixed layer, $t$ is time, $Q_{net}$ is the net SHF, $Q_{sw}(h)$ is the shortwave radiation that penetrates through the base of the mixed layer, $\rho = 1026$ kg m$^{-3}$ is seawater density, $c_p = 4200$ J kg$^{-1}$K$^{-1}$ is the specific heat capacity of seawater, $h$ is the mixed-layer depth, $(u_m, v_m)$ is the horizontal current velocity vertically averaged over the mixed layer, $w_e$ is entrainment velocity at the base of the mixed layer, and $T_h$ is potential temperature at the bottom of the mixed layer. The term DIFF represents diffusion. In our analysis, vertical advection and DIFF are treated together as residuals. The penetrative shortwave radiation at depth $h$ is parameterized following an exponential decay function (*73*)

$$Q_{sw}(h) \approx Q_{sw}(0) \left[ \alpha \, e^{-h/k_1} + (1-\alpha) e^{-h/k_2} \right] \quad (5)$$

where $Q_{sw}(0)$ is the surface shortwave radiation, $\alpha = 0.58$ is the fraction of energy in the longer-penetrating spectral band, $k_1 = 0.35$ m and $k_2 = 23$ m are the attenuation coefficients for the long and shortwave bands, respectively.

### Waveguide analysis: Stationary wavenumber and Rossby wave phase speed

The stationary wavenumber ($Ks$) and the Rossby wave phase speed ($c_p$) are fundamental parameters in atmospheric dynamics that describe the propagation and behavior of planetary waves. The stationary wavenumber $Ks$ is defined as (*74*)

$$Ks^2 = \frac{\beta^*}{U} \tag{6}$$

where $\beta^*$ is the effective meridional absolute vorticity gradient, given by

$$\beta^* = \beta - \frac{\partial^2 U}{\partial y^2} \tag{7}$$

where $\beta = \frac{df}{dy} = \frac{2\Omega\cos\phi}{a}$ is the planetary vorticity gradient, $\Omega$ is Earth's rotation rate, $\phi$ is latitude, $a$ is Earth's radius, and $U$ is the zonal wind speed. Equation 3 accounts for both planetary vorticity effects and the influence of the background wind curvature, making it more precise in determining the spatial scale of stationary Rossby waves. The $Ks$ represents the threshold for Rossby wave propagation: waves with zonal wavenumber $k < Ks$ propagate freely, whereas waves with $k > Ks$ decay; when $k \approx Ks$, waves propagate along the waveguide with minimal amplification or attenuation (*35*, *75*).

The Rossby wave phase speed ($c_p$) is given by

$$c_p = U - \frac{\beta}{k^2 + l^2} \tag{8}$$

where $k$ and $l$ are the zonal and meridional wavenumbers, respectively. In our analysis, we focus on purely zonal propagation by setting $l = 0$.

### Removing ENSO influence

To isolate the CGW's influence, we removed the ENSO impact by subtracting the linear regression patterns of each variable onto CTI from the original anomalies at each grid point, creating residual anomalies (denoted with asterisks) as follows

$$X^* = X - \gamma \cdot \mathrm{CTI} \tag{9}$$

where $X$ represents either SST, Z200, or V200, and $\gamma$ is the regression coefficient map of variable $X$ regressed onto the CTI index. This approach effectively removes the linear component of ENSO-related variability while preserving independent signals, including those associated with the CGW pattern.

### The first-order autoregressive AR(1) model

A first-order autoregressive AR(1) model is expressed as

$$\rho(k) = \alpha^k \rho(0) \tag{10}$$

where $\alpha$ represents the lag-1-month autocorrelation of the NWP index, $\rho(0)$ denotes the peak NWP-CGW correlation, and $k$ is the number of months after the peak. This model assumes that the decay of NWP SSTAs after the peak correlation with the CGW is governed by a first-order autoregressive process, where the memory of the system is determined by the lag-1-month autocorrelation coefficient $\alpha$.

### Barotropic energy conversion

To assess eddy-mean flow interactions in the winter wave train, we calculated the barotropic conversion term

$$\mathrm{CK} = -u'v' \ \partial\overline{u}/\partial y \quad -\left(u'2 - v'2\right) \ \partial\overline{u}/\partial x \tag{11}$$

where $u'$ and $v'$ are deviations from the zonal mean and $\overline{u}$ is the time-mean zonal-mean zonal wind. Negative CK indicates energy transfer from eddies to the mean flow, contributing to wave amplification; positive CK indicates energy transfer from the mean flow to eddies. Spatial smoothing (5 by 5 grid points) was applied before regression analysis to highlight large-scale patterns.

### Stochastic energy balance model

To validate the relationship between MLD and SST persistence, we applied a stochastic energy balance model framework. The ocean mixed-layer temperature evolution can be approximated by a first-order autoregressive process driven by stochastic atmospheric forcing and thermal damping

$$dT/dt = -\lambda T + F(t) \tag{12}$$

where $T$ is the SST anomaly, $\lambda$ is the damping coefficient, and $F(t)$ represents stochastic atmospheric forcing. The damping timescale $\tau = C/\lambda$, where $C = \rho c_p H$ is the heat capacity of the mixed layer, $\rho$ is seawater density, $c_p$ is specific heat capacity, and $H$ is the mixed-layer depth.

For monthly time steps ($\Delta t = 1$ month), the lag-1 autocorrelation $\alpha$ of SST anomalies is related to the damping timescale through

$$\alpha = e^{-\Delta t \cdot \frac{\lambda}{\rho c_p H}} \tag{13}$$

Taking the natural logarithm of both sides

$$\ln(\alpha) = -\Delta t \cdot \lambda / \left(\rho c_p H\right) \tag{14}$$

This shows that $\ln(\alpha)$ is inversely proportional to $H$. Therefore, for two regions with different MLD

$$\ln\left(\alpha_1\right) / \ln\left(\alpha_2\right) = H_2 / H_1 \tag{15}$$

we calculated the theoretical autocorrelation ratio using climatological MLD values and compared it with the observed lag-1 autocorrelations to validate that MLD differences explain the differential SST persistence.

### Forced AGCM experiments

We conducted forced AGCM experiments using the F1850 compset of CAM6 (*76*, *77*), configured with a horizontal resolution of ~2.5° longitude × 1.9° latitude and 30 vertical layers extending from the surface to 3.65 hPa. A total of three experiments were performed: a control (CTRL) run, and two sensitivity runs (NWP and NNA), each consisting of 10 ensemble members. In the CTRL run, monthly-varying climatological SST and sea ice data (*78*) were prescribed to drive CAM6. The NWP and NNA runs were forced with idealized Gaussian-shaped SST patterns (fig. S18). The NWP AGCM Run forcing center had a 2°C anomaly with an *e*-folding radius of 15° in the west-east (W-E) direction and 10° in the south-north (S-N) direction. The NNA AGCM Run forcing center had a 1°C anomaly with an *e*-folding radius of 15° in the W-E direction and 15° in the S-N direction. Each experiment was integrated for 2 years. The differences between the sensitivity runs and the CTRL run were analyzed to determine the atmospheric response to the prescribed SSTA forcing.

## Supplementary Materials

**This PDF file includes:**
Figs. S1 to S18
Tables S1 and S2

## REFERENCES


1. N. J. Holbrook, A. Sen Gupta, E. C. J. Oliver, A. J. Hobday, J. A. Benthuysen, H. A. Scannell, D. A. Smale, T. Wernberg, Keeping pace with marine heatwaves. *Nat. Rev. Earth Environ.* **1**, 482–493 (2020).
2. E. C. J. Oliver, J. A. Benthuysen, S. Darmaraki, M. G. Donat, A. J. Hobday, N. J. Holbrook, R. W. Schlegel, A. S. Gupta, Marine heatwaves. *Ann. Rev. Mar. Sci.* **13**, 313–342 (2021).
3. A. Capotondi, R. R. Rodrigues, A. Sen Gupta, J. A. Benthuysen, C. Deser, T. L. Frölicher, N. S. Lovenduski, D. J. Amaya, N. Le Grix, T. Xu, J. Hermes, N. J. Holbrook, C. Martinez-Villalobos, S. Masina, M. K. Roxy, A. Schaeffer, R. W. Schlegel, K. E. Smith, C. Wang, A global overview of marine heatwaves in a changing climate. *Commun. Earth Environ.* **5**, 1–17 (2024).
4. E. Di Lorenzo, N. Mantua, Multi-year persistence of the 2014/15 North Pacific marine heatwave. *Nat. Clim. Chang.* **6**, 1042–1047 (2016).
5. Y. Joh, E. Di Lorenzo, Increasing coupling between NPGO and PDO leads to prolonged marine heatwaves in the Northeast Pacific. *Geophys. Res. Lett.* **44**, 11663–11671 (2017).
6. Y. Zhao, J.-Y. Yu, Two marine heatwave (MHW) variants under a basinwide MHW conditioning mode in the North Pacific and their Atlantic associations. *J. Climate* **36**, 8657–8674 (2023).
7. A. J. Pershing, K. E. Mills, A. M. Dayton, B. S. Franklin, B. T. Kennedy, Evidence for adaptation from the 2016 marine heatwave in the Northwest Atlantic Ocean. *Oceanography* **31**, 152–161 (2018).
8. D. A. Smale, T. Wernberg, E. C. Oliver, M. Thomsen, B. P. Harvey, S. C. Straub, M. T. Burrows, L. V. Alexander, J. A. Benthuysen, M. G. Donat, Marine heatwaves threaten global biodiversity and the provision of ecosystem services. *Nat. Clim. Chang.* **9**, 306–312 (2019).
9. W. W. Cheung, T. L. Frölicher, Marine heatwaves exacerbate climate change impacts for fisheries in the northeast Pacific. *Sci. Rep.* **10**, 6678 (2020).
10. J. Garrabou, D. Gómez-Gras, A. Medrano, C. Cerrano, M. Ponti, R. Schlegel, N. Bensoussan, E. Turicchia, M. Sini, V. Gerovasileiou, N. Teixido, A. Mirasole, L. Tamburello, E. Cebrian, G. Rilov, J. Ledoux, J. B. Souissi, F. Khamassi, R. Ghanem, M. Benabdi, S. Grimes, O. Ocaña, H. Bazairi, B. Hereu, C. Linares, D. K. Kersting, G. La Rovira, J. Ortega, D. Casals, M. Pagès-Escolà, N. Margarit, P. Capdevila, J. Verdura, A. Ramos, A. Izquierdo, C. Barbera, E. Rubio-Portillo, I. Anton, P. López-Sendino, D. Díaz, M. Vázquez-Luis, C. Duarte, N. Marbà, E. Aspillaga, F. Espinosa, D. Grech, I. Guala, E. Azzurro, S. Farina, M. Cristina Gambi, G. Chimienti, M. Montefalcone, A. Azzola, T. P. Mantas, S. Fraschetti, G. Ceccherelli, S. Kipson, T. Bakran-Petricioli, D. Petricioli, C. Jimenez, S. Katsanevakis, I. T. Kizilkaya, Z. Kizilkaya, S. Sartoretto, R. Elodie, S. Ruitton, S. Comeau, J. Gattuso, J. Harmelin, Marine heatwaves drive recurrent mass mortalities in the Mediterranean Sea. *Glob. Chang. Biol.* **28**, 5708–5725 (2022).
11. D. G. Gomes, J. J. Ruzicka, L. G. Crozier, D. D. Huff, R. D. Brodeur, J. D. Stewart, Marine heatwaves disrupt ecosystem structure and function via altered food webs and energy flux. *Nat. Commun.* **15**, 1988 (2024).
12. D. J. Amaya, A. J. Miller, S.-P. Xie, Y. Kosaka, Physical drivers of the summer 2019 North Pacific marine heatwave. *Nat. Commun.* **11**, 1903 (2020).
13. Z.-A. Ge, L. Chen, T. Li, M. Sun, Unraveling the formation mechanism of exceptionally strong marine heatwaves in the Northeast Pacific in 2020. *J. Climate* **36**, 8091–8111 (2023).
14. N. A. Bond, M. F. Cronin, H. Freeland, N. Mantua, Causes and impacts of the 2014 warm anomaly in the NE Pacific. *Geophys. Res. Lett.* **42**, 3414–3420 (2015).
15. Z.-Z. Hu, A. Kumar, B. Jha, J. Zhu, B. Huang, Persistence and predictions of the remarkable warm anomaly in the northeastern Pacific Ocean during 2014–16. *J. Climate* **30**, 689–702 (2017).
16. Z. Chen, J. Shi, Q. Liu, H. Chen, C. Li, A persistent and intense marine heatwave in the Northeast Pacific during 2019–2020. *Geophys. Res. Lett.* **48**, e2021GL093239 (2021).
17. E. Behrens, D. Fernandez, P. Sutton, Meridional oceanic heat transport influences marine heatwaves in the Tasman Sea on interannual to decadal timescales. *Front. Mar. Sci.* **6**, 228 (2019).
18. E. N. S. Silva, B. T. Anderson, Northeast Pacific marine heatwaves linked to Kuroshio Extension variability. *Commun. Earth Environ.* **4**, 367 (2023).
19. D. J. Amaya, M. A. Alexander, A. Capotondi, C. Deser, K. B. Karnauskas, A. J. Miller, N. J. Mantua, Are long-term changes in mixed layer depth influencing North Pacific marine heatwaves? *Bull. Am. Meteorol. Soc.* **102**, S59–S66 (2021).
20. J. Shi, C. Tang, Q. Liu, Y. Zhang, H. Yang, C. Li, Role of mixed layer depth in the location and development of the Northeast Pacific warm blobs. *Geophys. Res. Lett.* **49**, e2022GL098849 (2022).
21. M. A. Alexander, I. Bladé, M. Newman, J. R. Lanzante, N.-C. Lau, J. D. Scott, The atmospheric bridge: The influence of ENSO teleconnections on air–sea interaction over the global oceans. *J. Climate* **15**, 2205–2231 (2002).
22. A. Capotondi, M. Newman, T. Xu, E. Di Lorenzo, An optimal precursor of Northeast Pacific marine heatwaves and Central Pacific el niño events. *Geophys. Res. Lett.* **49**, e2021GL097350 (2022).
23. H.-J. Hong, H.-H. Hsu, Remote tropical central Pacific influence on driving sea surface temperature variability in the Northeast Pacific. *Environ. Res. Lett.* **18**, 044005 (2023).
24. D. Li, Y. Chen, J. Qi, Y. Zhu, C. Lu, B. Yin, Attribution of the July 2021 record-breaking northwest Pacific marine heatwave to global warming, atmospheric circulation, and ENSO. *Bull. Am. Meteorol. Soc.* **104**, E291–E297 (2023).
25. H. Kuroda, T. Setou, Extensive marine heatwaves at the sea surface in the northwestern Pacific Ocean in summer 2021. *Remote Sens.* **13**, 3989 (2021).
26. D. L. Schumacher, M. Hauser, S. I. Seneviratne, Drivers and mechanisms of the 2021 Pacific Northwest heatwave. *Earth's Future* **10**, e2022EF002967 (2022).
27. E. Noh, J. Kim, S.-Y. Jun, G. Pak, J.-H. Kim, H.-G. Kim, Atmospheric pathway of marine heatwaves over the Northwestern Pacific. *Sci. Rep.* **13**, 22821 (2023).
28. Y. Kawakami, H. Nakano, L. S. Urakawa, T. Toyoda, K. Sakamoto, S. Nishikawa, T. Sugiyama, M. Kurogi, Y. Ishikawa, K. Sato, G. Yamanaka, Future changes in marine heatwaves based on high-resolution ensemble projections for the Northwestern Pacific Ocean. *J. Oceanogr.* **80**, 177–195 (2024).
29. S. Sugimoto, Marine heatwave off Tokai, Japan, attributed to the Kuroshio Large Meander Path, and an associated increase in summer rainfall over Japan. *J. Oceanogr.* **81**, 63–79 (2025).
30. Y. Yao, C. Wang, C. Wang, Record-breaking 2020 summer marine heatwaves in the western North Pacific. *Deep-Sea Res. II Top. Stud. Oceanogr.* **209**, 105288 (2023).
31. B. S. Giese, J. A. Carton, The seasonal cycle in coupled ocean-atmosphere model. *J. Climate* **7**, 1208–1217 (1994).
32. A. V. Fedorov, D. Cuff, A. Goudie, "Ocean–atmosphere coupling," in *Oxford Companion to Global Change* (Oxford Univ. Press, 2008), pp. 369–374.
33. Y.-C. Liang, J.-Y. Yu, E. S. Saltzman, F. Wang, Linking the tropical Northern Hemisphere pattern to the Pacific warm blob and Atlantic cold blob. *J. Climate* **30**, 9041–9057 (2017).
34. J. Shi, H. Huang, A. V. Fedorov, N. J. Holbrook, Y. Zhang, R. Ding, Y. Luo, S. Wang, J. Chen, X. Hu, Northeast Pacific warm blobs sustained via extratropical atmospheric teleconnections. *Nat. Commun.* **15**, 2832 (2024).
35. G. Branstator, Circumglobal teleconnections, the jet stream waveguide, and the North Atlantic Oscillation. *J. Climate* **15**, 1893–1910 (2002).
36. Q. Ding, B. Wang, Circumglobal teleconnection in the Northern Hemisphere summer. *J. Climate* **18**, 3483–3505 (2005).
37. W. Wang, W. Zhou, X. Wang, S. K. Fong, K. C. Leong, Summer high temperature extremes in Southeast China associated with the East Asian jet stream and circumglobal teleconnection. *JGR Atmospheres* **118**, 8306–8319 (2013).
38. H. Teng, G. Branstator, "Connections between heat waves and circumglobal teleconnection patterns in the Northern Hemisphere summer," in *Climate Extremes: Patterns and Mechanisms, Geophysical Monograph Series*, S.-Y. S. Wang, J. Yoon, C. C. Funk, R. R. Gillies, Eds. (Wiley, ed. 1, 2017), pp. 177–193; https://agupubs.onlinelibrary.wiley.com/doi/10.1002/9781119068020.ch11.
39. K. Kornhuber, S. Osprey, D. Coumou, S. Petri, V. Petoukhov, S. Rahmstorf, L. Gray, Extreme weather events in early summer 2018 connected by a recurrent hemispheric wave-7 pattern. *Environ. Res. Lett.* **14**, 054002 (2019).
40. K. Kornhuber, D. Coumou, E. Vogel, C. Lesk, J. F. Donges, J. Lehmann, R. M. Horton, Amplified Rossby waves enhance risk of concurrent heatwaves in major breadbasket regions. *Nat. Clim. Chang.* **10**, 48–53 (2020).
41. Q. Lin, J. Yuan, Linkages between amplified quasi-stationary waves and humid heat extremes in Northern Hemisphere midlatitudes. *J. Climate* **35**, 8245–8258 (2022).
42. M. G. Jacox, M. A. Alexander, D. Amaya, E. Becker, S. J. Bograd, S. Brodie, E. L. Hazen, M. Pozo Buil, D. Tommasi, Global seasonal forecasts of marine heatwaves. *Nature* **604**, 486–490 (2022).
43. H. Wang, Y. Lu, L. Zhai, X. Chen, S. Liu, Variations of surface marine heatwaves in the Northwest Pacific during 1993–2019. *Front. Mar. Sci.* **11**, 1323702 (2024).
44. H. Sato, K. Takemura, A. Ito, T. Umeda, S. Maeda, Y. Tanimoto, M. Nonaka, H. Nakamura, Impact of an unprecedented marine heatwave on extremely hot summer over Northern Japan in 2023. *Sci. Rep.* **14**, 16100 (2024).
45. B. Huang, X. Yin, J. A. Carton, L. Chen, G. Graham, P. Hogan, T. Smith, H.-M. Zhang, Record high sea surface temperatures in 2023. *Geophys. Res. Lett.* **51**, e2024GL108369 (2024).
46. Z.-Z. Hu, M. J. McPhaden, B. Huang, J. Zhu, Y. Liu, Accelerated warming in the North Pacific since 2013. *Nat. Clim. Chang.* **14**, 929–931 (2024).
47. F. Thoral, S. Montie, M. S. Thomsen, L. W. Tait, M. H. Pinkerton, D. R. Schiel, Unravelling seasonal trends in coastal marine heatwave metrics across global biogeographical realms. *Sci. Rep.* **12**, 7740 (2022).

48. C. S. Y. Huang, N. Nakamura, Local finite-amplitude wave activity as a diagnostic of anomalous weather events. *J. Atmos. Sci.* **73**, 211–229 (2016).
49. D. Coumou, V. Petoukhov, S. Rahmstorf, S. Petri, H. J. Schellnhuber, Quasi-resonant circulation regimes and hemispheric synchronization of extreme weather in boreal summer. *Proc. Natl. Acad. Sci. U.S.A.* **111**, 12331–12336 (2014).
50. N. Nakamura, C. S. Y. Huang, Atmospheric blocking as a traffic jam in the jet stream. *Science* **361**, 42–47 (2018).
51. B. Hoskins, T. Woollings, Persistent extratropical regimes and climate extremes. *Curr. Clim. Change Rep.* **1**, 115–124 (2015).
52. J. S. A. Green, A problem in baroclinic stability. *Q. J. Roy. Meteorol. Soc.* **86**, 237–251 (1960).
53. J.-S. Lin, B. Wu, T.-J. Zhou, Is the interdecadal circumglobal teleconnection pattern excited by the Atlantic multidecadal Oscillation? *Atmos. Ocean. Sci. Lett.* **9**, 451–457 (2016).
54. S. Tang, S. Qiao, B. Wang, F. Liu, X. Zhu, T. Feng, G. Feng, W. Dong, Recent changes in ENSO's impacts on the summertime circumglobal teleconnection and mid-latitude extremes. *Nat. Commun.* **16**, 646 (2025).
55. Q. Ding, B. Wang, Intraseasonal teleconnection between the summer Eurasian wave train and the Indian monsoon. *J. Climate* **20**, 3751–3767 (2007).
56. X. Sun, Q. Ding, S.-Y. S. Wang, D. Topál, Q. Li, C. Castro, H. Teng, R. Luo, Y. Ding, Enhanced jet stream waviness induced by suppressed tropical Pacific convection during boreal summer. *Nat. Commun.* **13**, 1288 (2022).
57. E. A. Barnes, J. A. Screen, The impact of Arctic warming on the midlatitude jet-stream: Can it? Has it? Will it? *WIREs Clim. Change* **6**, 277–286 (2015).
58. D. Coumou, G. Di Capua, S. Vavrus, L. Wang, S. Wang, The influence of Arctic amplification on mid-latitude summer circulation. *Nat. Commun.* **9**, 2959 (2018).
59. S. Undorf, M. A. Bollasina, G. C. Hegerl, Impacts of the 1900–74 increase in anthropogenic aerosol emissions from North America and Europe on Eurasian Summer Climate. *J. Climate* **31**, 8381–8399 (2018).
60. F. Liu, X. Li, Y. Luo, W. Cai, J. Lu, X.-T. Zheng, S. M. Kang, H. Wang, L. Zhou, Increased Asian aerosols drive a slowdown of Atlantic meridional overturning circulation. *Nat. Commun.* **15**, 18 (2024).
61. J. A. Francis, S. J. Vavrus, Evidence for a wavier jet stream in response to rapid Arctic warming. *Environ. Res. Lett.* **10**, 014005 (2015).
62. T. L. Frölicher, C. Laufkötter, Emerging risks from marine heat waves. *Nat. Commun.* **9**, 650 (2018).
63. H. Shi, F.-F. Jin, R. C. J. Wills, M. G. Jacox, D. J. Amaya, B. A. Black, R. R. Rykaczewski, S. J. Bograd, M. García-Reyes, W. J. Sydeman, Global decline in ocean memory over the 21st century. *Sci. Adv.* **8**, eabm3468 (2022).
64. D. Coumou, J. Lehmann, J. Beckmann, The weakening summer circulation in the Northern Hemisphere mid-latitudes. *Science* **348**, 324–327 (2015).
65. M. E. Mann, S. Rahmstorf, K. Kornhuber, B. A. Steinman, S. K. Miller, S. Petri, D. Coumou, Projected changes in persistent extreme summer weather events: The role of quasi-resonant amplification. *Sci. Adv.* **4**, eaat3272 (2018).
66. N. A. Rayner, D. E. Parker, E. B. Horton, C. K. Folland, L. V. Alexander, D. P. Rowell, E. C. Kent, A. Kaplan, Global analyses of sea surface temperature, sea ice, and night marine air temperature since the late nineteenth century. *J. Geophys. Res.* **108**, 2002JD002670 (2003).
67. E. Kalnay, M. Kanamitsu, R. Kistler, W. Collins, D. Deaven, L. Gandin, M. Iredell, S. Saha, G. White, J. Woollen, Y. Zhu, M. Chelliah, W. Ebisuzaki, W. Higgins, J. Janowiak, K. C. Mo, C. Ropelewski, J. Wang, A. Leetmaa, R. Reynolds, R. Jenne, D. Joseph, The NCEP/NCAR 40-year reanalysis project. *Bull. Am. Meteorol. Soc.* **77**, 437–471 (1996).
68. D. W. Behringer, M. Ji, A. Leetmaa, An improved coupled model for ENSO prediction and implications for ocean initialization. Part I: The ocean data assimilation system. *Mon. Weather Rev.* **126**, 1013–1021 (1998).
69. V. Eyring, S. Bony, G. A. Meehl, C. A. Senior, B. Stevens, R. J. Stouffer, K. E. Taylor, Overview of the Coupled Model Intercomparison Project Phase 6 (CMIP6) experimental design and organization. *Geosci. Model Dev.* **9**, 1937–1958 (2016).
70. G. P. Compo, J. S. Whitaker, P. D. Sardeshmukh, N. Matsui, R. J. Allan, X. Yin, B. E. Gleason, R. S. Vose, G. Rutledge, P. Bessemoulin, S. Brönnimann, M. Brunet, R. I. Crouthamel, A. N. Grant, P. Y. Groisman, P. D. Jones, M. C. Kruk, A. C. Kruger, G. J. Marshall, M. Maugeri, H. Y. Mok, Ø. Nordli, T. F. Ross, R. M. Trigo, X. L. Wang, S. D. Woodruff, S. J. Worley, The twentieth century reanalysis project. *Q. J. R. Meteorol. Soc.* **137**, 1–28 (2011).
71. F. W. Zwiers, H. Von Storch, Taking serial correlation into account in tests of the mean. *J. Climate* **8**, 336–351 (1995).
72. M. F. Cronin, N. A. Bond, J. Thomas Farrar, H. Ichikawa, S. R. Jayne, Y. Kawai, M. Konda, B. Qiu, L. Rainville, H. Tomita, Formation and erosion of the seasonal thermocline in the Kuroshio Extension Recirculation Gyre. *Deep-Sea Res. II Top. Stud. Oceanogr.* **85**, 62–74 (2013).
73. C. A. Paulson, J. J. Simpson, Irradiance measurements in the upper ocean. *J. Phys. Oceanogr.* **7**, 952–956 (1977).
74. N. Harnik, R. S. Lindzen, The effect of reflecting surfaces on the vertical structure and variability of stratospheric planetary waves. *J. Atmos. Sci.* **58**, 2872–2894 (2001).
75. B. J. Hoskins, T. Ambrizzi, Rossby wave propagation on a realistic longitudinally varying flow. *J. Atmos. Sci.* **50**, 1661–1671 (1993).
76. A. Gettelman, M. J. Mills, D. E. Kinnison, R. R. Garcia, A. K. Smith, D. R. Marsh, S. Tilmes, F. Vitt, C. G. Bardeen, J. McInerny, H.-L. Liu, S. C. Solomon, L. M. Polvani, L. K. Emmons, J.-F. Lamarque, J. H. Richter, A. S. Glanville, J. T. Bacmeister, A. S. Phillips, R. B. Neale, I. R. Simpson, A. K. DuVivier, A. Hodzic, W. J. Randel, The whole atmosphere community climate model version 6 (WACCM6). *J. Geophys. Res. Atmos.* **124**, 12380–12403 (2019).
77. G. Danabasoglu, J.-F. Lamarque, J. Bacmeister, D. A. Bailey, A. K. DuVivier, J. Edwards, L. K. Emmons, J. Fasullo, R. Garcia, A. Gettelman, C. Hannay, M. M. Holland, W. G. Large, P. H. Lauritzen, D. M. Lawrence, J. T. M. Lenaerts, K. Lindsay, W. H. Lipscomb, M. J. Mills, R. Neale, K. W. Oleson, B. Otto-Bliesner, A. S. Phillips, W. Sacks, S. Tilmes, L. van Kampenhout, M. Vertenstein, A. Bertini, J. Dennis, C. Deser, C. Fischer, B. Fox-Kemper, J. E. Kay, D. Kinnison, P. J. Kushner, V. E. Larson, M. C. Long, S. Mickelson, J. K. Moore, E. Nienhouse, L. Polvani, P. J. Rasch, W. G. Strand, The community earth system model version 2 (CESM2). *J. Adv. Model. Earth Syst.* **12**, e2019MS001916 (2020).
78. J. W. Hurrell, J. J. Hack, D. Shea, J. M. Caron, J. Rosinski, A new sea surface temperature and sea ice boundary dataset for the Community Atmosphere Model. *J. Climate* **21**, 5145–5153 (2008).

**Acknowledgments:** We thank the reviewers whose constructive comments greatly improved the analysis and clarity of this manuscript. We gratefully acknowledge the institutions and data centers that provided the observational datasets and model outputs used in this study. High-performance computing resources were provided by the National Center for Atmospheric Research (NCAR) Computational and Information Systems Laboratory, sponsored by the National Science Foundation. **Funding:** This research was funded by the Climate and Large-Scale Dynamics Program of the US National Science Foundation grant AGS-2109539 (J.-Y.Y.) and NASA Award NNH19ZHA001C to the California Space Grant Consortium (CalSpace) (Y.Z.). **Author contributions:** Conceptualization: Y.Z. and J.-Y.Y. Methodology: Y.Z. and J.-Y.Y. Investigation: Y.Z. and J.-Y.Y. Formal analysis: Y.Z. Validation: Y.Z. and J.-Y.Y. Data curation: Y.Z. Software: Y.Z. Visualization: Y.Z. Resources: Y.Z. and J.-Y.Y. Funding acquisition: Y.Z. and J.-Y.Y. Writing—original draft: Y.Z. and J.-Y.Y. Writing—review and editing: Y.Z. and J.-Y.Y. Supervision: J.-Y.Y. Project administration: J.-Y.Y. **Competing interests:** The authors declare that they have no competing interests. **Data, code, and materials availability:** All data and code needed to evaluate and reproduce the results in the paper are present in the paper and/or the Supplementary Materials. The Hadley Centre Sea Ice and SST data are available at www.metoffice.gov.uk/hadobs/hadisst/. The National Centers for Environmental Prediction/National Center for Atmospheric Research Reanalysis 1 data are available at https://psl.noaa.gov/data/gridded/data.ncep.reanalysis.html. The Twentieth Century Reanalysis Project dataset version 3 is available at https://psl.noaa.gov/data/gridded/data.20thC_ReanV3.html. The Global Ocean Data Assimilation System (GODAS) dataset is available at www.esrl.noaa.gov/psd/data/gridded/data.godas.html. The falwa Python package for LWA calculations is available at https://github.com/csyhuang/hn2016_falwa. The Community Atmosphere Model version 6 (CAM6) is freely available as part of the Community Earth System Model (CESM) project at www.cesm.ucar.edu/models/cesm2. The codes used to generate all figures are archived on Zenodo (https://doi.org/10.5281/zenodo.18883906) and GitHub (https://github.com/YuZhao1998/NWP-MHW-with-CGW/tree/master). The CAM6 model output data generated in this study are available from the corresponding author J.-Y.Y. (jyyu@uci.edu) upon reasonable request. This study did not generate new materials.

Submitted 2 June 2025
Accepted 21 May 2026
Published 3 July 2026
10.1126/sciadv.adz4647

Science Advances

# Trans-basin linkages prolong Northwestern Pacific marine heatwaves through a circumglobal wave pattern

Yu Zhao and Jin-Yi Yu

*Sci. Adv.* **12** (27), eadz4647. DOI: 10.1126/sciadv.adz4647



*Science Advances* (ISSN 2375-2548) is published by the American Association for the Advancement of Science. 1200 New York Avenue NW, Washington, DC 20005. The title *Science Advances* is a registered trademark of AAAS.

Science Advances
AAAS

# Supplementary Materials for

## Trans-basin linkages prolong Northwestern Pacific marine heatwaves through a circumglobal wave pattern

Yu Zhao and Jin-Yi Yu

Corresponding author: Jin-Yi Yu, jyyu@uci.edu

*Sci. Adv.* **12**, eadz4647 (2026)
DOI: 10.1126/sciadv.adz4647

**This PDF file includes:**

Figs. S1 to S18
Tables S1 and S2

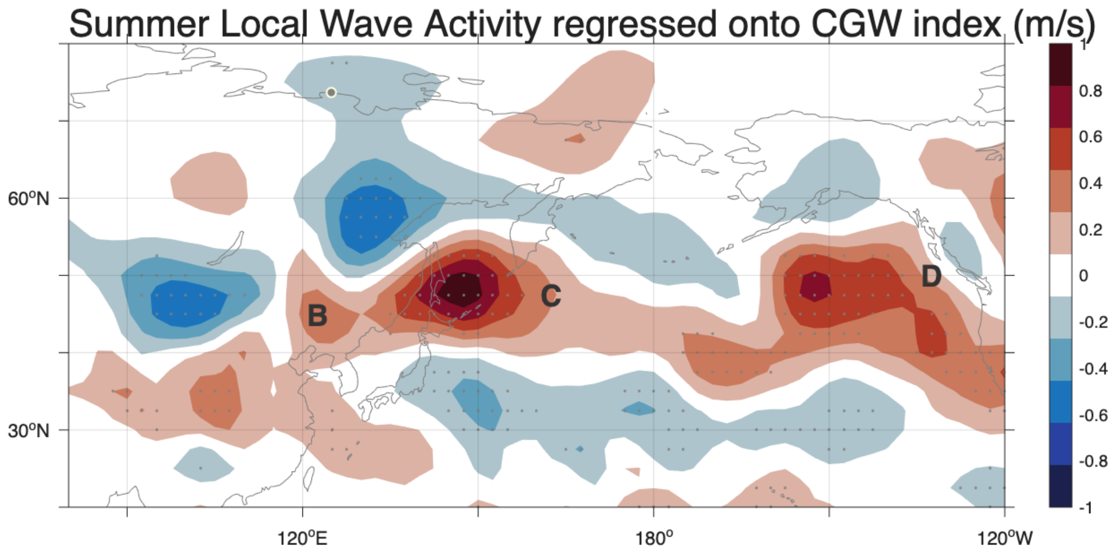


**Figure S1. Local Wave Activity confirms separate wave packets at B and C.** Summer (JJA) Local Wave Activity at 200 hPa regressed onto the CGW index. Gray dots indicate 95% significance.

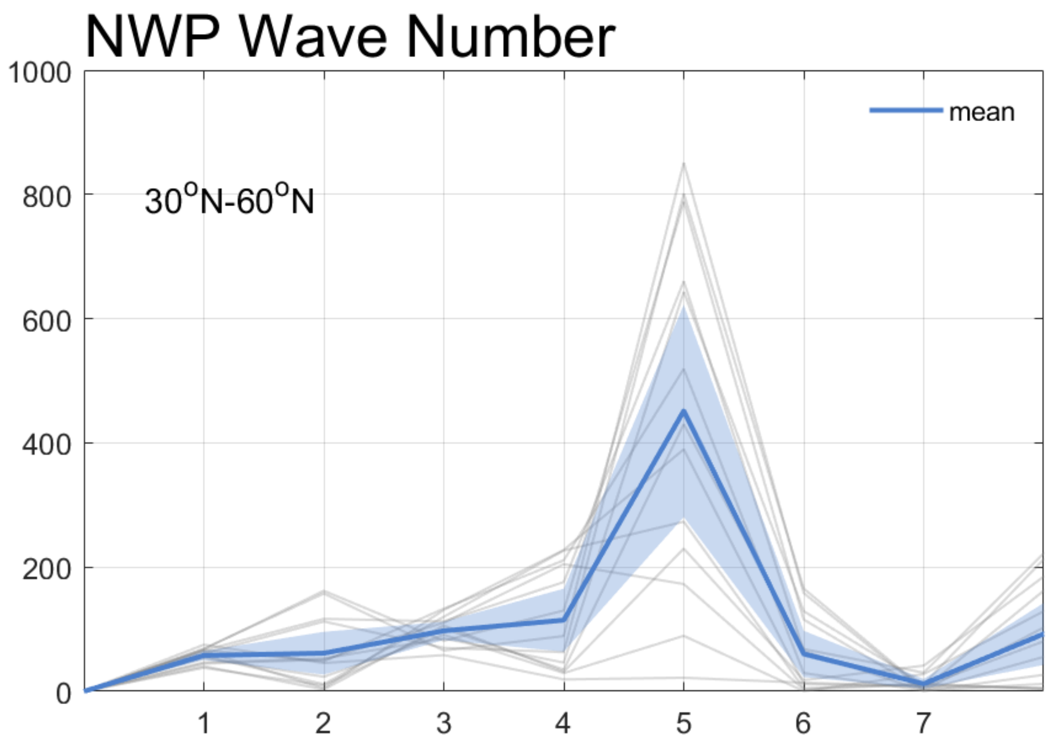


**Figure S2. Zonal wave number spectrum of the Circumglobal Wave (CGW) pattern.** The zonal wave number spectrum is derived from meridional wind (30°N–60°N) anomalies regressed onto the late summer NWP index, with ENSO signals removed (see Methods). The blue line shows the spectrum averaged across the 30°N–60°N latitude band, with light blue shading indicating the 95% confidence interval. Gray lines represent spectra at individual latitudes within this band (2.5° intervals), highlighting the dominant wavenumber-5 structure consistent with the five high-pressure centers observed in the CGW pattern.

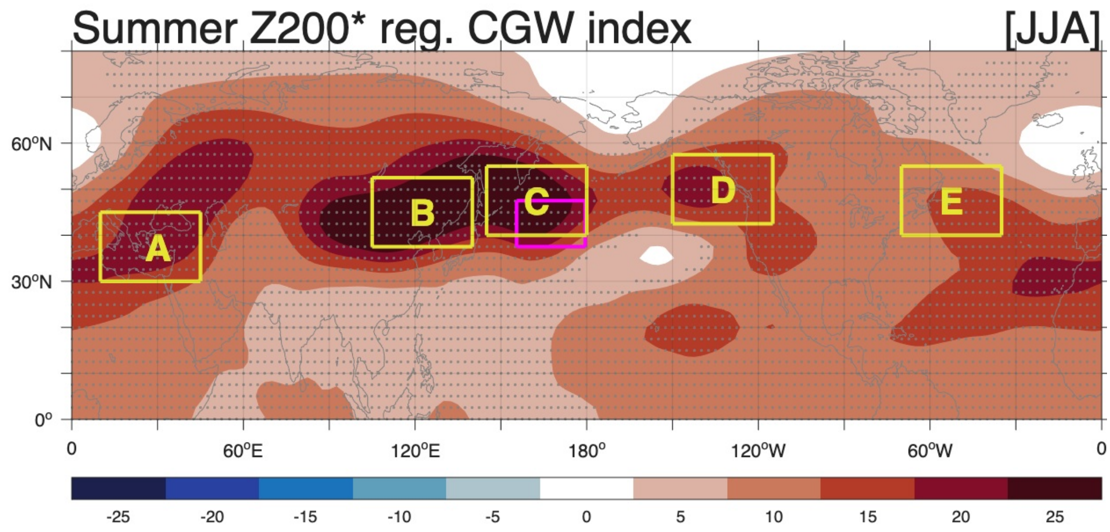


**Figure S3. The Circumglobal Wave pattern revealed by the CGW index.** Summer (JJA) Z200* anomalies (Z200 with ENSO influences removed; see Methods) regressed of onto the summer CGW index, highlighting five High centers labeled A–E (yellow boxes). The Northwestern Pacific (NWP) region is outlined in a magenta box. Gray dots indicate areas statistically significant at the 95% confidence level.

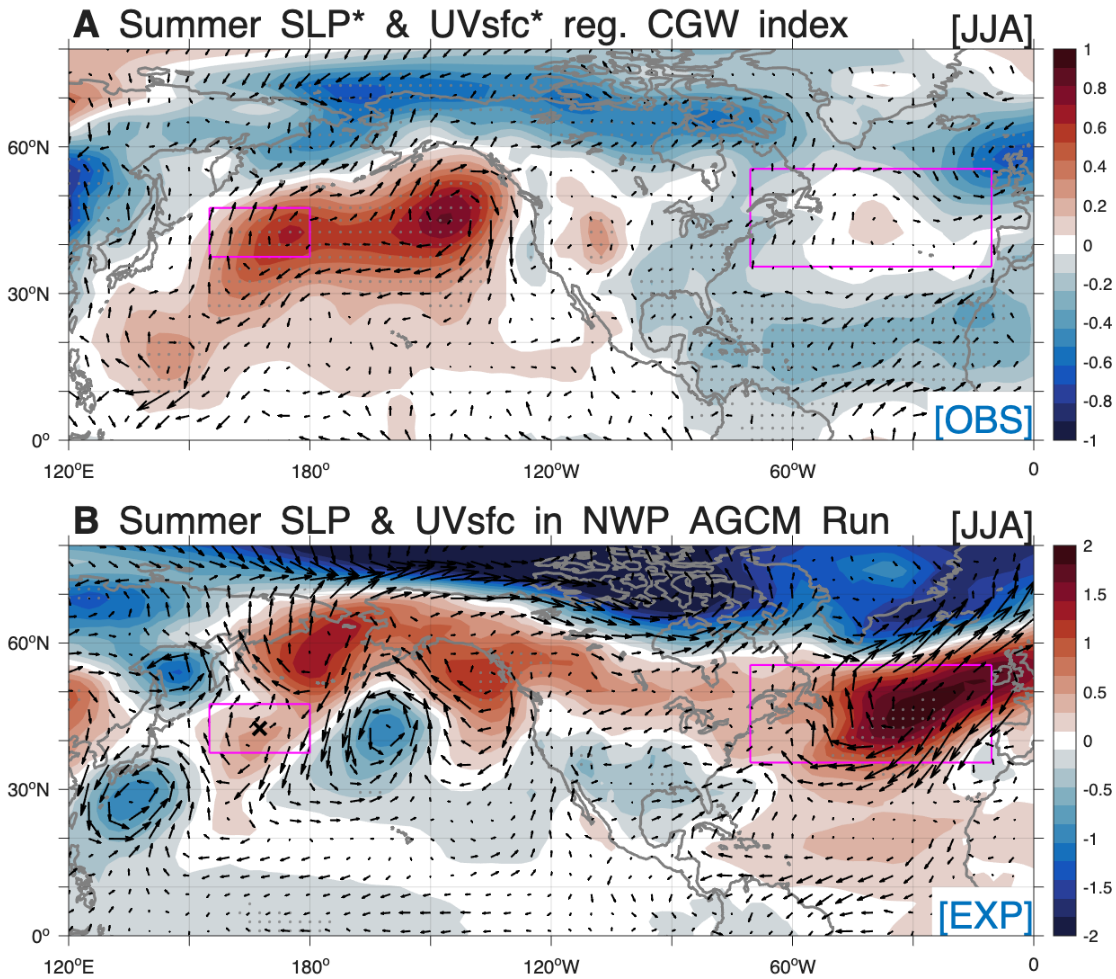


**Figure S4. Surface expression of the Circumglobal Wave pattern. A** Summer (JJA) sea-level pressure anomalies (SLP*, hPa, shading) and surface wind anomalies (UVsfc, vectors, m/s) regressed onto the summer CGW index from observations. **B** Summer surface wind response (vectors, m/s) and SLP anomalies (shading, hPa) in the NWP Run of forced AGCM experiment. The magenta boxes indicate the NWP region, and the forcing center is marked by '**x**' in panel **B**.

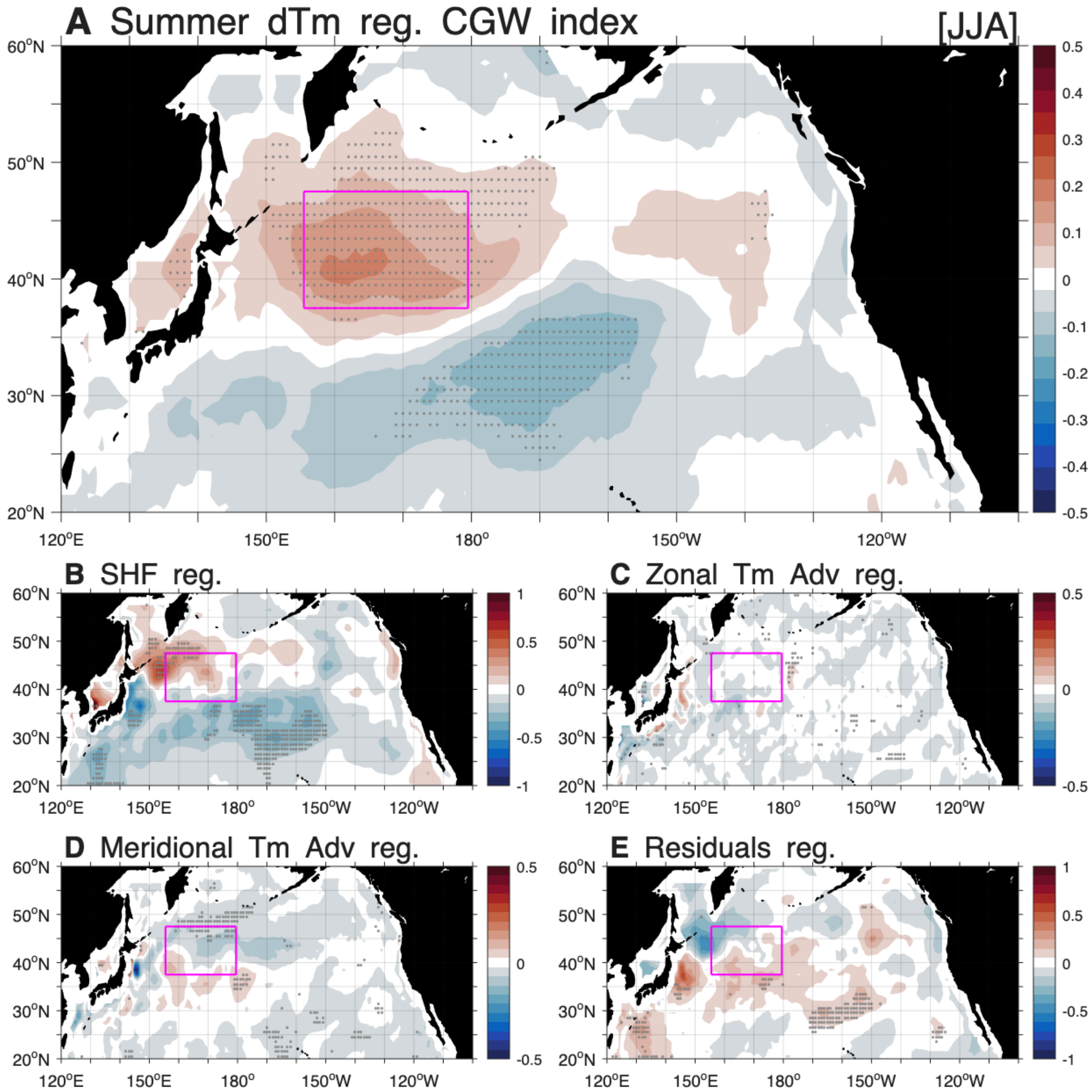


**Figure S5. Summer ocean mixed-layer heat budget with the Circumglobal Wave pattern in North Pacific.** **A** Regression of summer ocean mixed-layer temperature tendency (dTm) onto the CGW index. **B** Regression of surface heat flux (SHF) onto the CGW index. **C** Regression of zonal Tm transport onto the CGW index. **D** Regression of meridional Tm transport onto the CGW index. **E** Regression of residuals onto the CGW index. Statistical significance at the 95% confidence level is indicated by gray dots. The NWP region is marked by magenta boxes. All panels show temperature tendency terms in units of °C/month.

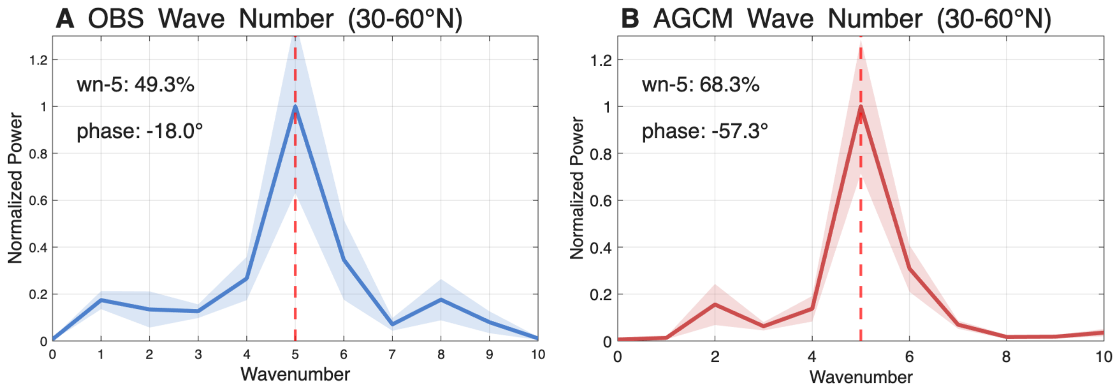


**Figure S6. Wavenumber spectrum validation for AGCM NWP simulation.** Same as Fig. S2 but for the wave patterns shown in Fig. 3C and D. Both observations **A** and AGCM simulation **B** show dominant wavenumber-5 structure (49.3% and 68.3% of variance, respectively), with phases of −18.0° and −57.3°.

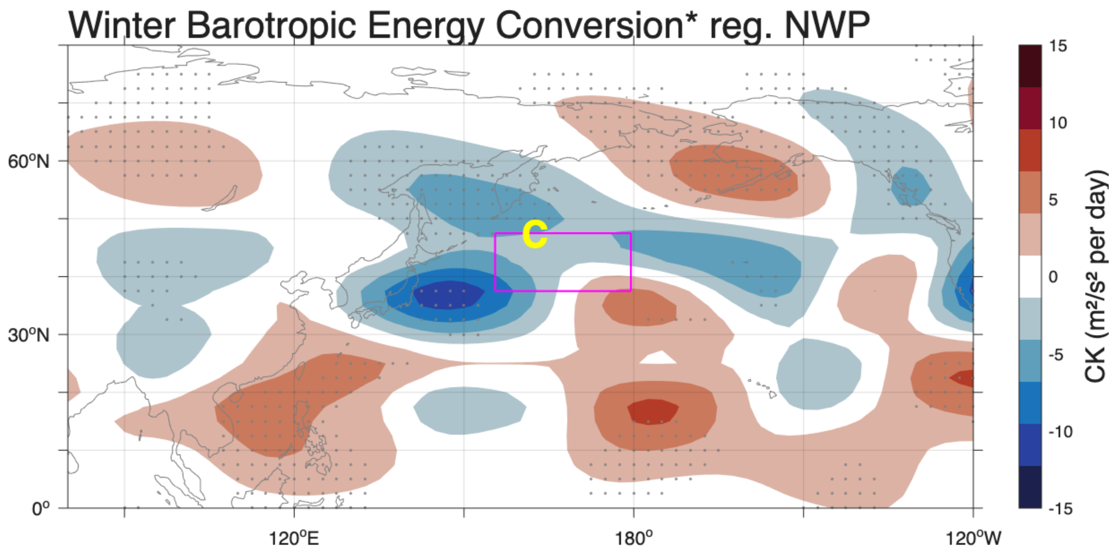


**Figure S7. Barotropic energy conversion associated with the winter NWP wave train.** Winter (DJF) barotropic energy conversion (CK, with ENSO signal removed) regressed onto the winter NWP index. The yellow letter "C" marks the CGW-C center, and the magenta box indicates the NWP region. Gray dots denote statistical significance at the 95% confidence level.

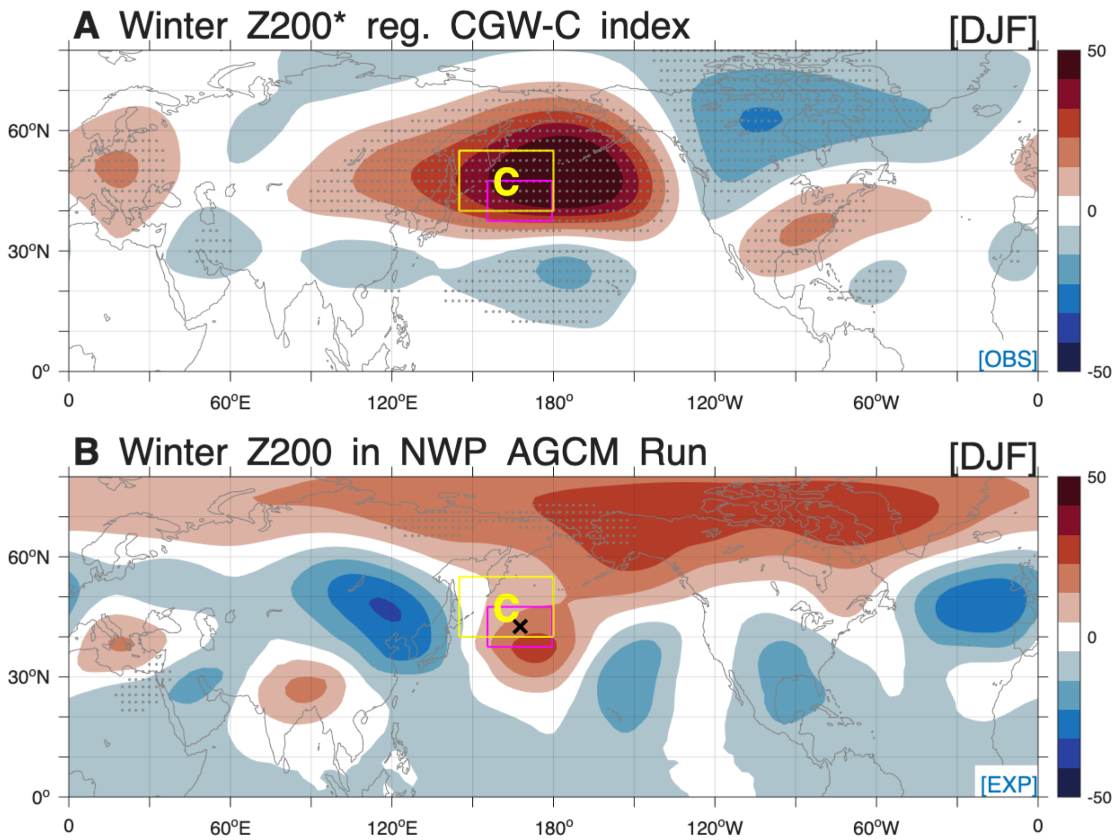


**Figure S8. The winter atmospheric patterns associated with Northwestern Pacific marine heatwaves. A** Winter (DJF) Z200* (Z200 anomalies with ENSO signal removed) regression onto the CGW-C index. **B** Winter Z200 anomalies response in the NWP Run of forced AGCM experiment. The prescribed SSTA forcing center in the AGCM experiment is marked by '**x**'. The CGW-C region is marked by the yellow box labeled "C", and the magenta box indicates the NWP region. Statistical significance at the 95% confidence level is indicated by gray dots.

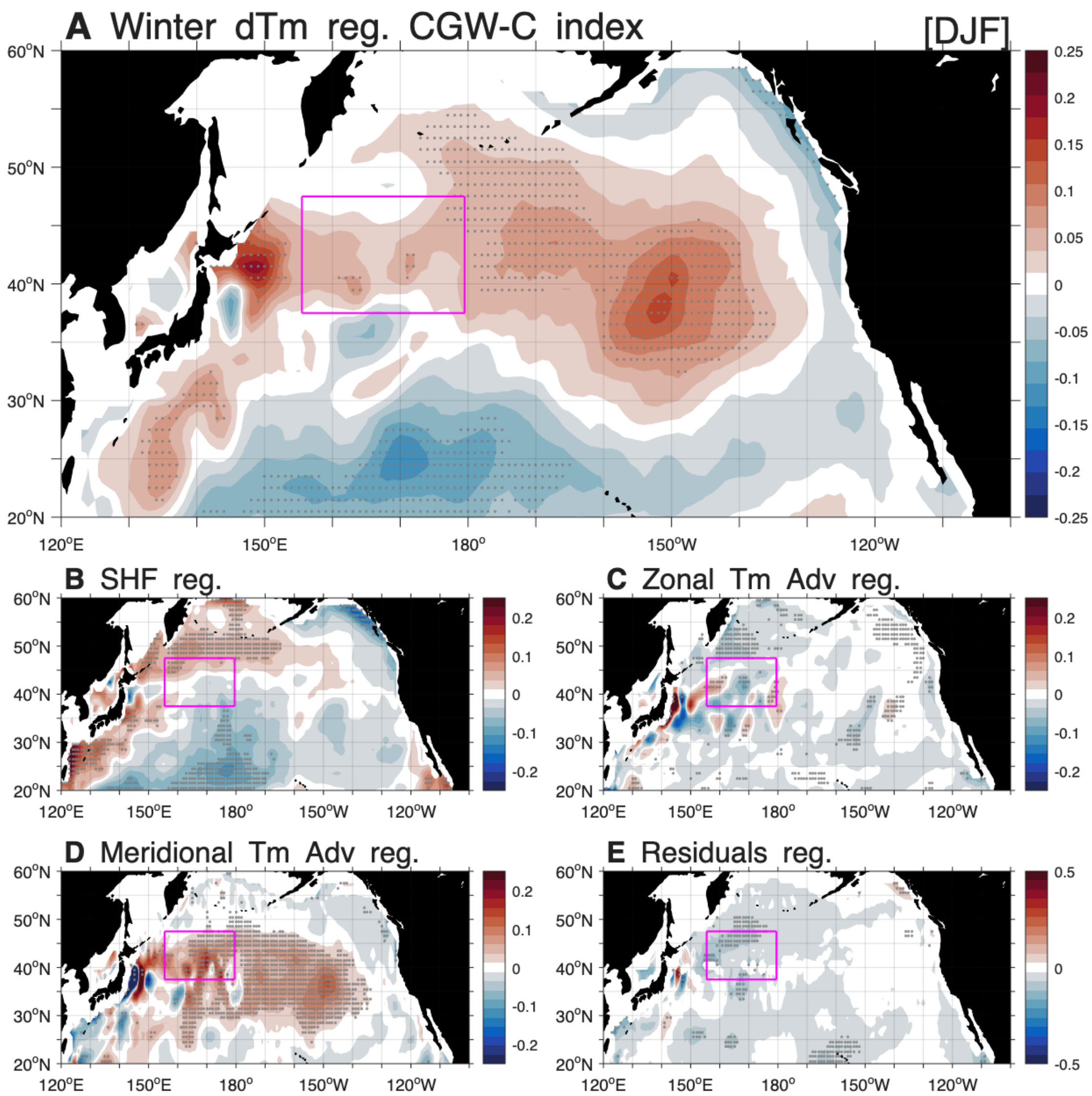


**Figure S9. Winter ocean mixed layer heat budget with the Circumglobal Wave pattern in North Pacific.** Same as Fig. S5 but for regressions against the CGW-C index (see Methods) instead of the full CGW index in winter (DJF).

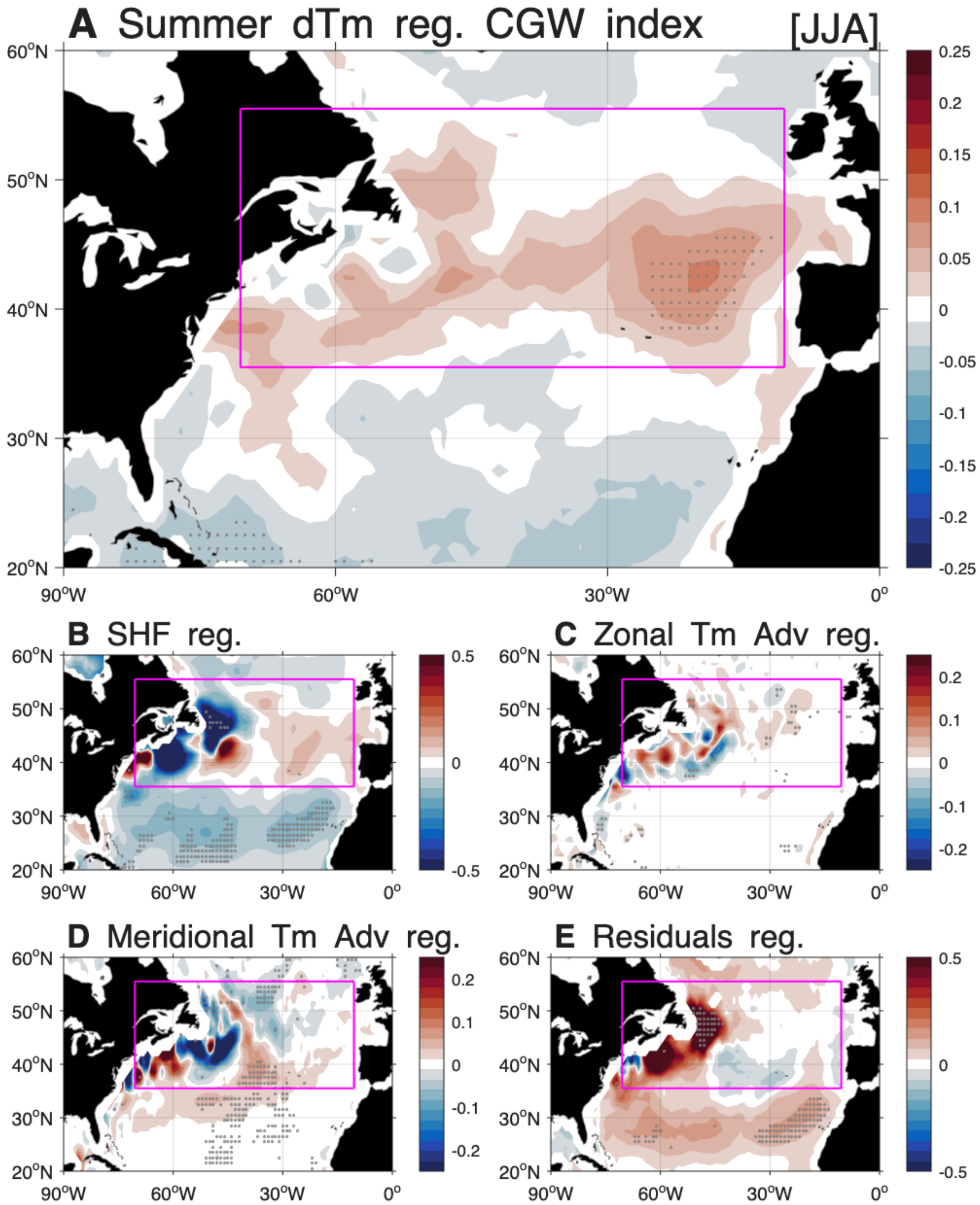


**Figure S10. Summer ocean mixed-layer heat budget in the North Atlantic region.** Same as Fig. S5 but for regressions onto the summer CGW index in the North Atlantic sector. The magenta box indicates the NNA region.

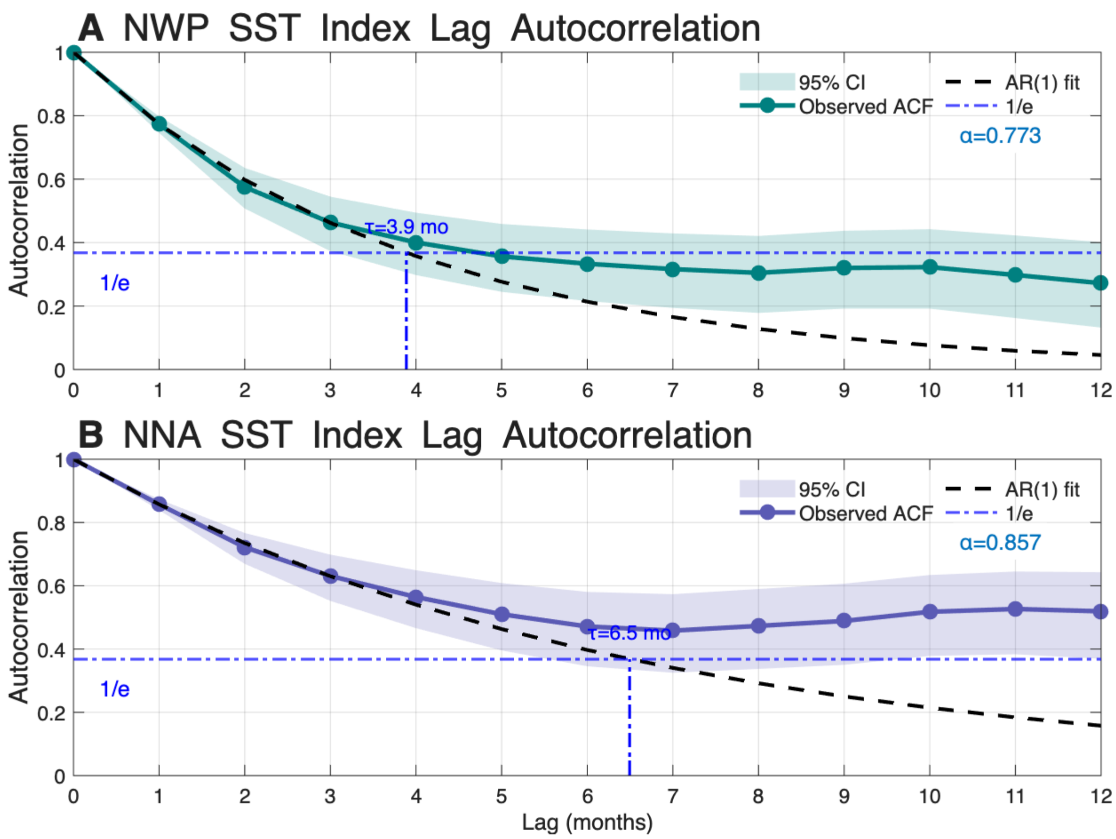


**Figure S11. Differential SST persistence between NWP and NNA regions.** Lag autocorrelation of monthly SST indices for **A** NWP and **B** NNA regions. Solid lines show observed autocorrelation functions with 95% confidence intervals (shading). Dashed lines show AR(1) model fits with lag-1 autocorrelation $\alpha = 0.773$ (NWP) and $\alpha = 0.857$ (NNA). Horizontal dash-dot lines indicate 1/e threshold, with vertical dashed lines marking e-folding times of 3.9 months (NWP) and 6.5 months (NNA).

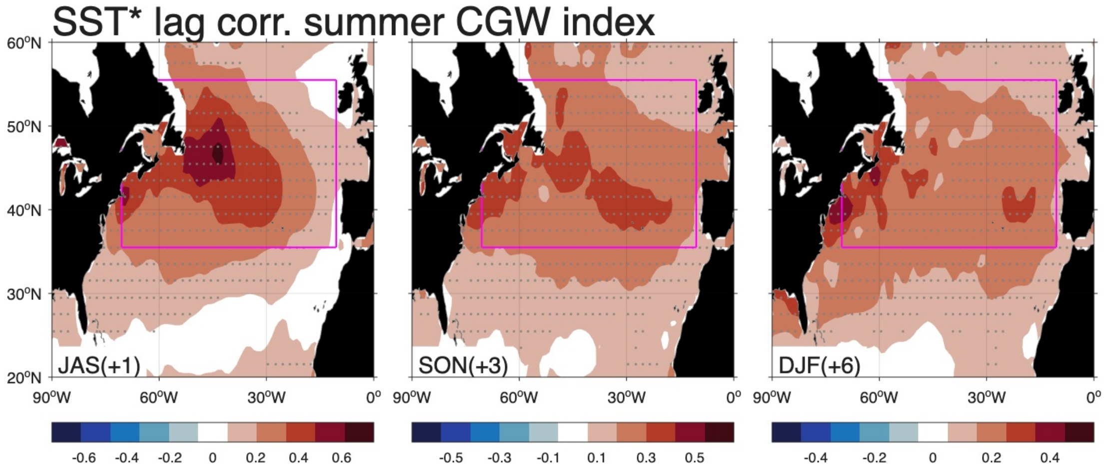


**Figure S12. Seasonal persistence of North Atlantic warming, driven by the summer CGW pattern.** SST* (SST anomalies with ENSO signal removed) lag correlation with the summer CGW index across seasons: JAS(+1), SON(+3), and DJF(+6). The magenta boxes denote the NNA region. Gray dots indicate statistical significance at the 95% confidence level.

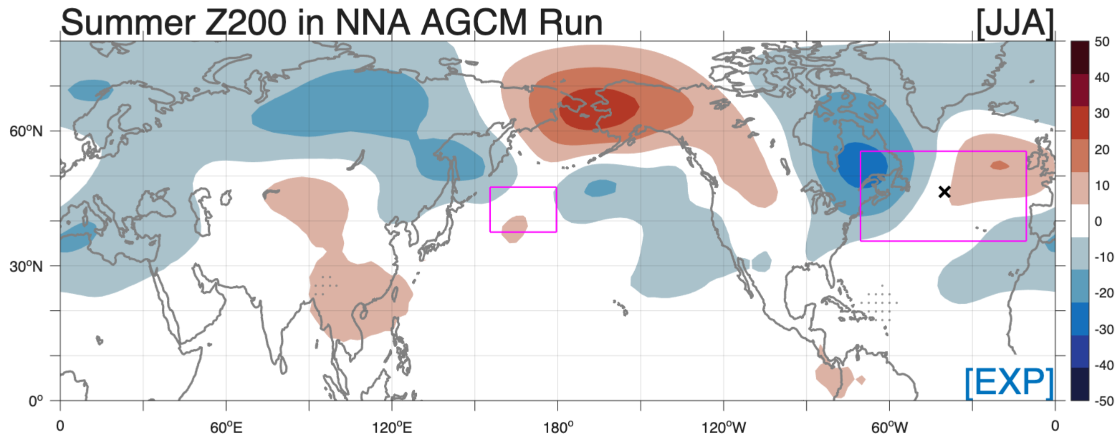


**Figure S13. Summer atmospheric response to North Atlantic warming in AGCM experiment.** Summer (JJA) Z200 anomalies (m) in the NNA AGCM experiment relative to the control run. The magenta boxes indicate the NWP and NNA regions. The black cross marks the NNA SST forcing center. Stippling indicates statistical significance at the 95% confidence level.

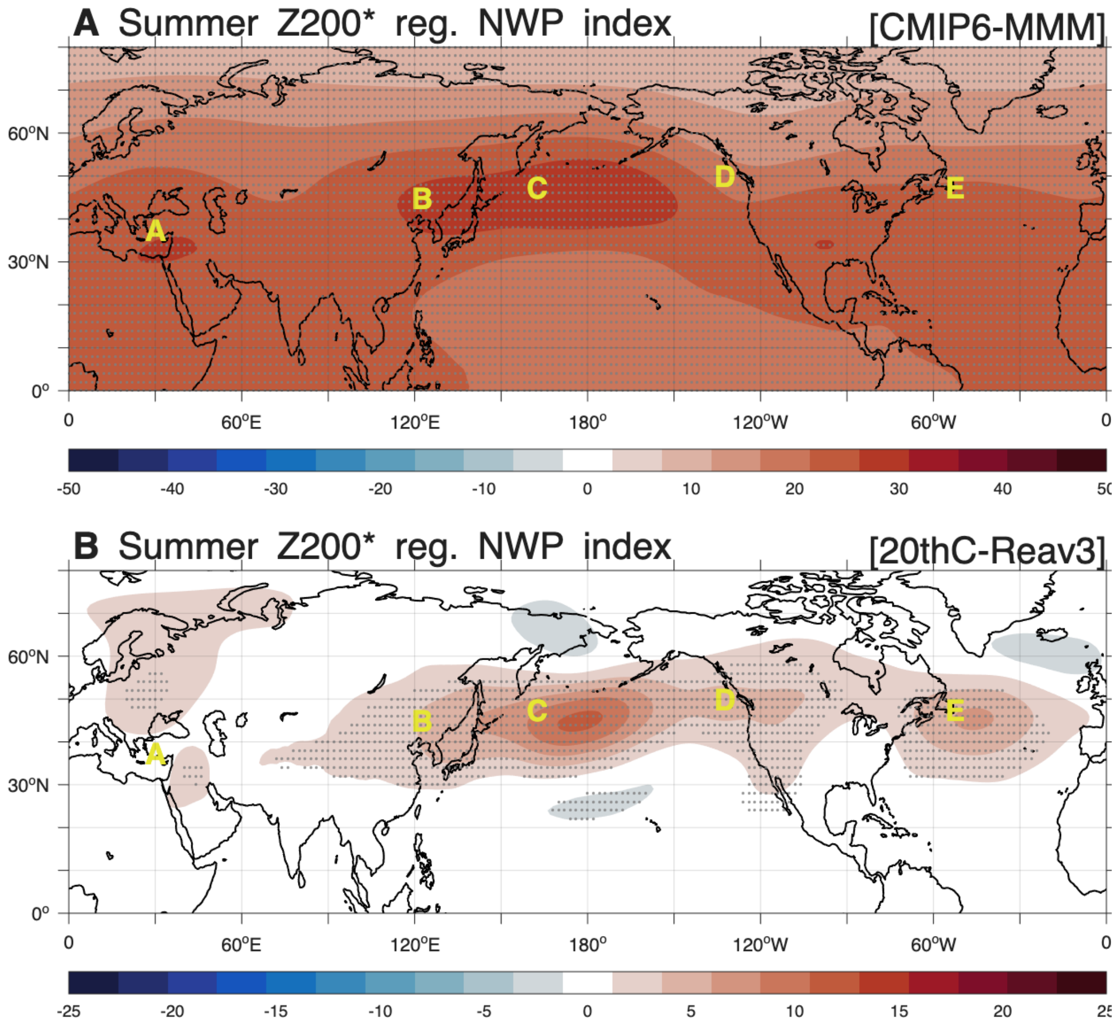


**Figure S14. CGW patterns as the driver of NWP SSTA in CMIP6 multi-model mean and 20th Century Reanalysis.** **A** CMIP6 multi-model mean (CMIP6-MMM) and **B** 20th Century Reanalysis V3 (20thC-Reav3) showing summer (JJA) Z200* (Z200 anomalies with ENSO signal removed) regression onto the NWP index. The CGW centers (A–E), identified from Fig. 1C, are indicated by yellow labels. Statistical significance at the 95% confidence level is indicated by gray dots.

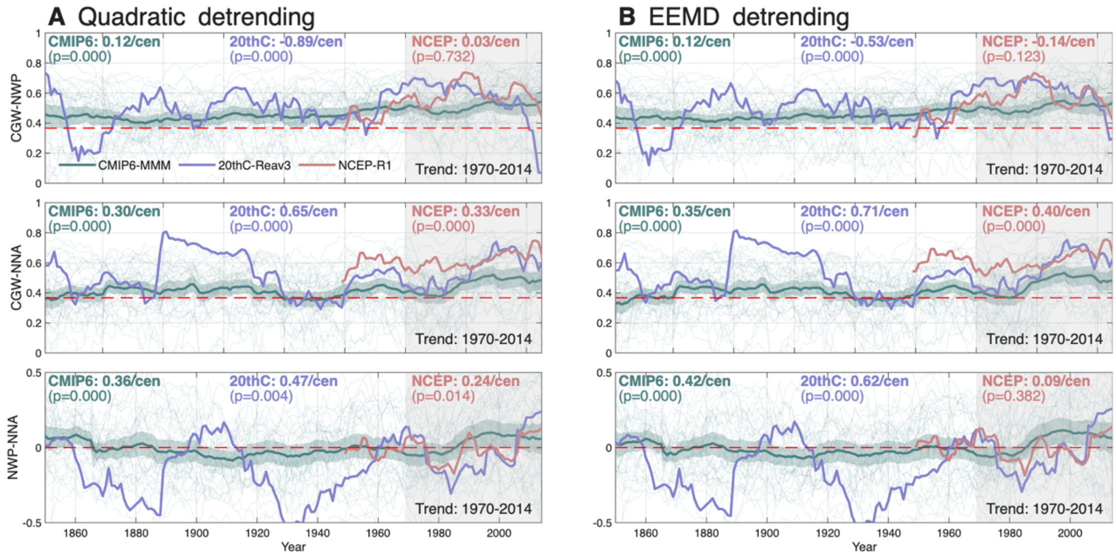


**Figure S15. Robustness of strengthening CGW–MHW relationships to different detrending methods.** 30-year running correlations between detrended indices using **A** quadratic detrending and **B** Ensemble Empirical Mode Decomposition (EEMD) detrending. Top row: summer CGW–NWP correlation; middle row: summer CGW–NNA correlation; bottom row: winter NWP–NNA correlation. Green lines show CMIP6 multi-model mean (CMIP6-MMM) with shading indicating 95% confidence interval, purple lines show 20th Century Reanalysis V3 (20thC-Reav3), and pink lines show NCEP/NCAR Reanalysis 1 (NCEP-R1). Light green lines represent individual CMIP6 models. Trend values (per century) and p-values for 1970–2014 are labeled in each panel. Red dashed lines indicate the critical correlation coefficient at 95% confidence level.

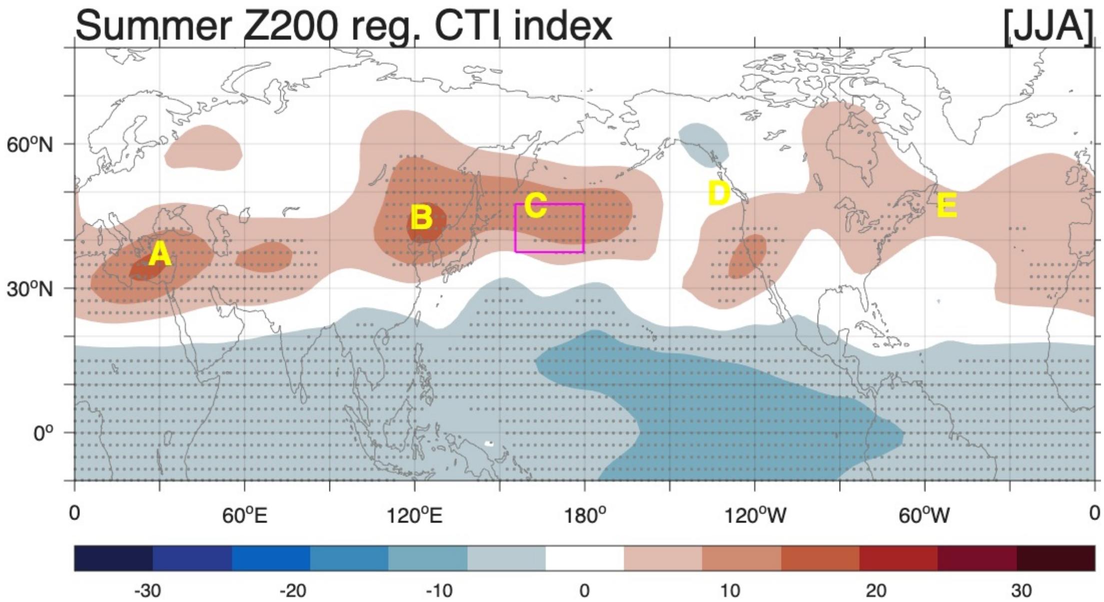


**Figure S16. The summer atmospheric pattern driven by ENSO forcing.** Summer (JJA) Z200 regression against the CTI (cold tongue index; multiplied by −1 for comparison). The CGW centers (A–E), identified from Fig. 1C, are indicated by yellow labels. The magenta box indicates the NWP region. Statistical significance at the 95% confidence level is indicated by gray dots.

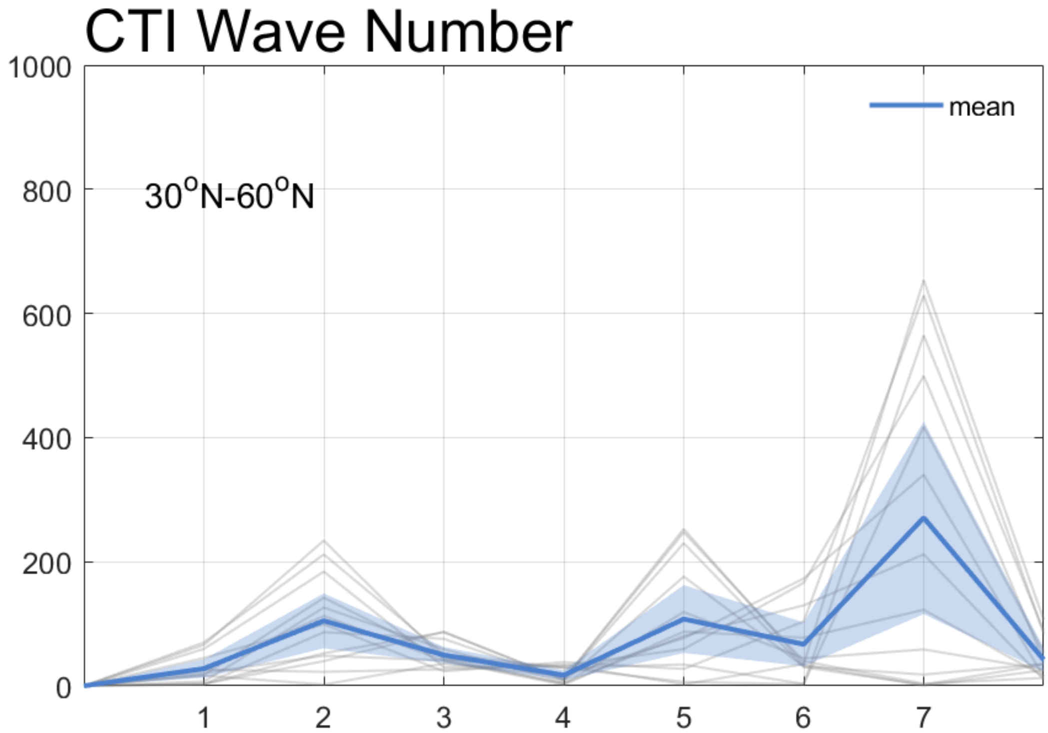


**Figure S17. Zonal wave number spectrum of the Cold Tongue Index (CTI) atmospheric pattern.** The zonal wave number spectrum is derived from meridional wind (30°N–60°N) anomalies regressed onto the summer CTI index. The blue line shows the spectrum averaged across the 30°N–60°N latitude band, with light blue shading indicating the 95% confidence interval. Gray lines represent spectra at individual latitudes within this band (2.5° intervals). Unlike the CGW pattern (Fig. S3), the CTI-associated atmospheric response shows a broader spectral distribution with less pronounced wavenumber-5 dominance.

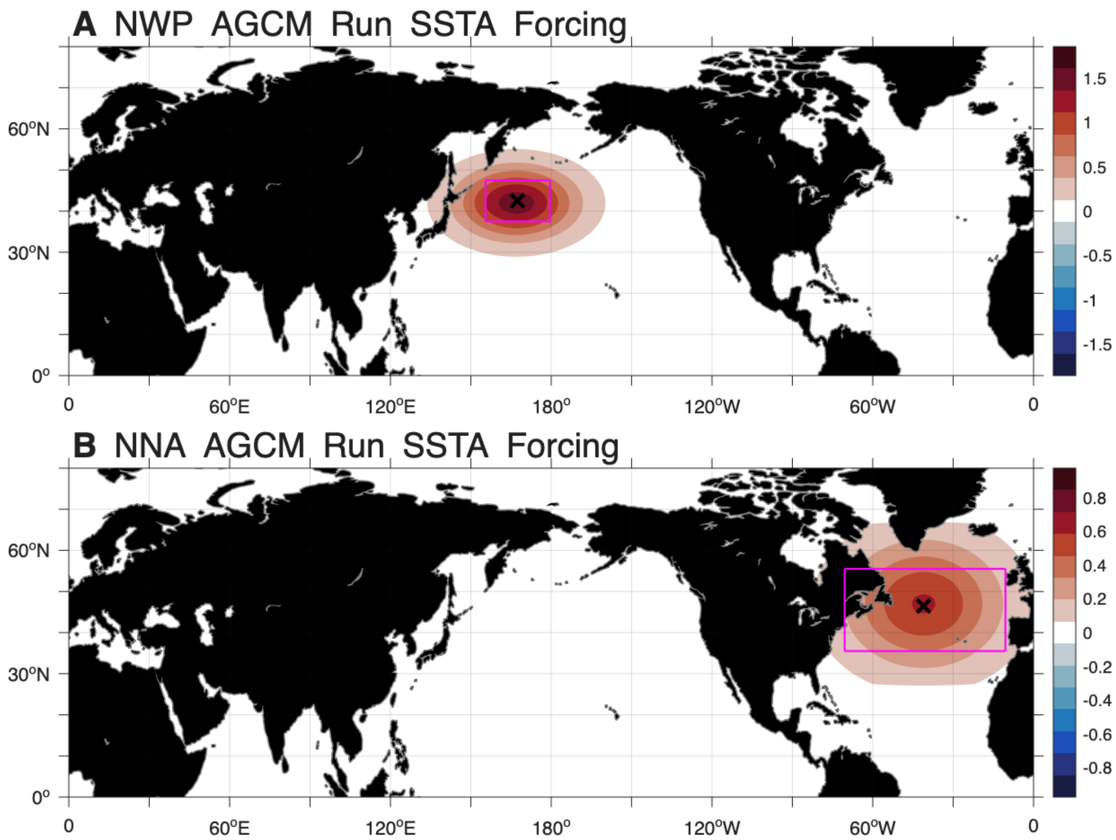


**Figure S18. SST anomaly forcing used in the AGCM experiments. A** The prescribed SSTA forcing for the NWP AGCM Run experiments, with a warming anomaly with forcing center (marked by '**x**') at 42.5°N, 167.5°E, having east–west e-folding radius of ~15° and north–south e-folding radius of ~10°. The magenta box indicates the NWP region. **B** The prescribed SSTA forcing for the NNA AGCM Run experiments, with a warming anomaly centered at 45°N, 40°W (marked by '**x**'), having east–west e-folding radius of ~15° and north–south e-folding radius of ~15°. The magenta box indicates the NNA region.

**Table S1. CMIP6 Models Used in This Study.** List of Coupled Model Intercomparison Project Phase 6 (CMIP6) models whose historical simulations were analyzed in this study, along with their configurations. All model outputs were remapped to 1° × 1° spatial resolution for the historical period 1850–2014, using ensemble member r1i1p1f1.

| *Model Name* | *Institution* | *Atmospheric Model* | *Ocean Model* |
|---|---|---|---|
| AWI-CM-1-1-MR | Alfred Wegener Institute | ECHAM6.3 | FESOM1.4 |
| AWI-ESM-1-1-LR | Alfred Wegener Institute | ECHAM6.3 | FESOM1.4 |
| BCC-CSM2-MR | Beijing Climate Center | BCC AGCM3-MR | MOM4 |
| BCC-ESM1 | Beijing Climate Center | BCC AGCM2.1 | MOM4 |
| CAMS-CSM1-0 | Chinese Academy of Meteorological Sciences | CAM5.3 | MOM4 |
| CESM2-FV2 | National Center for Atmospheric Research (NCAR) | CAM6 (FV2 grid) | POP2 (FV2 grid) |
| CESM2-WACCM-FV2 | NCAR | WACCM6 (FV2 grid) | POP2 (FV2 grid) |
| CESM2-WACCM | NCAR | WACCM6 | POP2 |
| CESM2 | NCAR | CAM6 | POP2 |
| CMCC-CM2-HR4 | Euro-Mediterranean Center on Climate Change | CAM4.1 | NEMO3.6 |
| CMCC-CM2-SR5 | Euro-Mediterranean Center on Climate Change | CAM4.1 | NEMO3.6 |
| CMCC-ESM2 | Euro-Mediterranean Center on Climate Change | CAM4.1 | NEMO3.6 |
| CanESM5 | Canadian Centre for Climate Modelling & Analysis | CanAM5 | CanOM5 |
| E3SM-1-0 | DOE & | EAM (v1.0) | MPAS-Ocean |

| | | | |
|---|---|---|---|
| | Collaborators | | (v1.0) |
| E3SM-1-1-ECA | DOE & Collaborators | EAM (v1.1) | MPAS-Ocean (v1.1) |
| E3SM-1-1 | DOE & Collaborators | EAM (v1.1) | MPAS-Ocean (v1.1) |
| EC-Earth3-Veg-LR | EC-Earth Consortium | IFS cy36r4 | NEMO3.6 |
| FGOALS-f3-L | Chinese Academy of Sciences | CAS FGOALS-f3-L AGCM | LICOM3 |
| FGOALS-g3 | Chinese Academy of Sciences | GAMIL3 | LICOM3 |
| FIO-ESM-2-0 | First Institute of Oceanography | SAMIL3 | NEMO3.6 |
| GFDL-CM4 | NOAA Geophysical Fluid Dynamics Laboratory | GFDL-AM4.0.1 | GFDL-MOM6.0.1 |
| GFDL-ESM4 | NOAA Geophysical Fluid Dynamics Laboratory | GFDL-AM4.0.1 | GFDL-MOM6.0.1 |
| GISS-E2-1-G-CC | NASA Goddard Institute for Space Studies | GISS-E2.1G | HYCOM |
| GISS-E2-1-G | NASA Goddard Institute for Space Studies | GISS-E2.1G | HYCOM |
| GISS-E2-1-H | NASA Goddard Institute for Space Studies | GISS-E2.1H | HYCOM |
| IITM-ESM | Indian Institute of Tropical Meteorology | IITM-ESM-AM | MOM4p1 |
| INM-CM4-8 | Institute for Numerical Mathematics | INM-AM4.8 | INM-OM5 |
| INM-CM5-0 | Institute for Numerical Mathematics | INM-AM5.0 | INM-OM5.0 |
| IPSL-CM6A-LR-INCA | Institut Pierre-Simon Laplace | LMDZ (6A-NH) | NEMO3.6 |
| IPSL-CM6A-LR | Institut Pierre-Simon Laplace | LMDZ (6A) | NEMO3.6 |

| | | | |
|---|---|---|---|
| KIOST-ESM | Korea Institute of Ocean Science & Technology | KIOST-AGCM | NEMO3.6 |
| MCM-UA-1-0 | University of Arizona | CAM4 | MOM5 |
| MIROC6 | Japan Agency for Marine-Earth Science & Tech | MIROC-AGCM | MRI.COM4.4 |
| MPI-ESM-1-2-HAM | Max Planck Institute for Meteorology | ECHAM6.3 | MPIOM1.6 |
| MPI-ESM1-2-HR | Max Planck Institute for Meteorology | ECHAM6.3 | MPIOM1.6 (High-Res) |
| MPI-ESM1-2-LR | Max Planck Institute for Meteorology | ECHAM6.3 | MPIOM1.6 (Low-Res) |
| MRI-ESM2-0 | Meteorological Research Institute | MRI-AGCM3.5 | MRI.COM4.4 |
| NESM3 | Nanjing University of Information Science & Tech | CAM5.3 | NEMO3.6 |
| NorCPM1 | Norwegian Climate Centre | CAM-OSLO | MICOM |
| NorESM2-LM | Norwegian Climate Centre | CAM6 | MICOM |
| NorESM2-MM | Norwegian Climate Centre | CAM6 | MICOM (Medium Res) |
| SAM0-UNICON | Seoul National University | SAM0 (CAM6 with Unified Conv) | POP2 |
| TaiESM1 | Academia Sinica (Taiwan) | TaiAM1 (CAM5.3 modified) | NEMO3.6 |

**Table S2. Sensitivity of correlation trends to detrending methods.** Trends in 30-year running correlations from 1970–2014 (per century) for different index pairs, datasets, and detrending methods. Asterisks indicate statistical significance: *** $p < 0.001$, ** $p < 0.01$, * $p < 0.05$.

| Dataset | Index Pair | Linear | Quadratic | EEMD |
|---|---|---|---|---|
| CMIP6-MMM | CGW-NWP | 0.34*** | 0.12*** | 0.12*** |
| | CGW-NNA | 0.59*** | 0.30*** | 0.35*** |
| | NWP-NNA | 0.63*** | 0.36*** | 0.42*** |
| 20thC-Reav3 | CGW-NWP | -0.03 | -0.89*** | -0.53*** |
| | CGW-NNA | 1.04*** | 0.65*** | 0.71*** |
| | NWP-NNA | 0.79*** | 0.47** | 0.62*** |
| NCEP-R1 | CGW-NWP | 0.12 | 0.03 | -0.14 |
| | CGW-NNA | 0.45*** | 0.33*** | 0.40*** |
| | NWP-NNA | 0.18 | 0.24* | 0.09 |

*Note: CGW–NWP and CGW–NNA represent summer (JJA) relationships; NWP–NNA represents winter (DJF) relationships.*